

An intercomparison and evaluation of aircraft-derived and simulated CO from seven chemical transport models during the TRACE-P experiment

Christopher M. Kiley,¹ Henry E. Fuelberg,¹ Paul I. Palmer,² Dale J. Allen,³ Gregory R. Carmichael,⁴ Daniel J. Jacob,^{2,8} Celine Mari,⁵ R. Bradley Pierce,⁶ Kenneth E. Pickering,³ Youhua Tang,⁴ Oliver Wild,⁷ T. Duncan Fairlie,^{6,8} Jennifer A. Logan,⁸ Glen W. Sachse,⁶ Todd K. Shaack,⁹ and David G. Streets¹⁰

Received 29 October 2002; revised 14 March 2003; accepted 26 March 2003; published 15 November 2003.

[1] Four global scale and three regional scale chemical transport models are intercompared and evaluated during NASA's Transport and Chemical Evolution over the Pacific (TRACE-P) experiment. Model simulated and measured CO are statistically analyzed along aircraft flight tracks. Results for the combination of 11 flights show an overall negative bias in simulated CO. Biases are most pronounced during large CO events. Statistical agreements vary greatly among the individual flights. Those flights with the greatest range of CO values tend to be the worst simulated. However, for each given flight, the models generally provide similar relative results. The models exhibit difficulties simulating intense CO plumes. CO error is found to be greatest in the lower troposphere. Convective mass flux is shown to be very important, particularly near emissions source regions. Occasionally meteorological lift associated with excessive model-calculated mass fluxes leads to an overestimation of middle and upper tropospheric mixing ratios. Planetary Boundary Layer (PBL) depth is found to play an important role in simulating intense CO plumes. PBL depth is shown to cap plumes, confining heavy pollution to the very lowest levels. *INDEX TERMS*: 0341 Atmospheric Composition and Structure: Middle atmosphere—constituent transport and chemistry (3334); 0345 Atmospheric Composition and Structure: Pollution—urban and regional (0305); 0365 Atmospheric Composition and Structure: Troposphere—composition and chemistry; 0368 Atmospheric Composition and Structure: Troposphere—constituent transport and chemistry

Citation: Kiley, C. M., et al., An intercomparison and evaluation of aircraft-derived and simulated CO from seven chemical transport models during the TRACE-P experiment, *J. Geophys. Res.*, 108(D21), 8819, doi:10.1029/2002JD003089, 2003.

¹Department of Meteorology, Florida State University, Tallahassee, Florida, USA.

²Division of Engineering and Applied Sciences, Harvard University, Cambridge, Massachusetts, USA.

³Department of Meteorology, University of Maryland, College Park, Maryland, USA.

⁴Center for Global and Regional Environmental Research and Department of Chemical and Biochemical Engineering, University of Iowa, Iowa City, Iowa, USA.

⁵Laboratoire d'Aerologie, UMR CNRS/Universite Paul Sabatier, Toulouse, France.

⁶NASA Langley Research Center, Hampton, Virginia, USA.

⁷Frontier Research System for Global Change, Yokohama, Japan.

⁸Department of Earth and Planetary Sciences, Harvard University, Cambridge, Massachusetts, USA.

⁹Space Science and Engineering Center, University of Wisconsin, Madison, Wisconsin, USA.

¹⁰Argonne National Laboratory, Argonne, Illinois, USA.

1. Introduction

[2] NASA's Transport and Chemical Evolution over the Pacific (TRACE-P) experiment, conducted between February and April 2001, sought to characterize the chemical composition of Asian outflow and describe its evolution over the Pacific Basin. The goals of TRACE-P were to improve our knowledge of the Asian sources of climatically important atmospheric species and to understand the implications for global atmospheric budgets [Jacob *et al.*, 2003]. In addition to in situ chemical measurements by two NASA aircraft (a DC-8 and P-3B), TRACE-P included a major support activity from several three-dimensional (3-D) chemical transport models (CTMs) that were used in real time to optimize flight strategies.

[3] Many evaluations of individual CTMs have been conducted previously [e.g., Allen *et al.*, 1996a, 1996b; Bey *et al.*, 2001; Wild and Prather, 2000]. However, very few intercomparisons of different CTMs appear in the literature. Jacob *et al.* [1997] performed a model intercomparison of radon simulations, while Kanakidou *et al.* [1999] evaluated carbon monoxide as a tracer. Rasch *et al.* [2000]

compared simulations of radon, lead, sulfur dioxide, and sulfate, and *Carmichael et al.* [2002] evaluated the long-range transport of sulfur deposition. The large number of 3-D CTMs run during TRACE-P provides a unique opportunity to determine how the transport simulations compare among themselves and with observations. That was the goal of this research.

[4] Seven 3-D CTMs that were run during TRACE-P participated in the intercomparison. They differ in several ways including domain size, resolution, meteorological fields, and their approaches and detail for simulating chemical processes and deposition.

[5] Carbon monoxide, a tracer common to all seven models, was selected as the intercomparison species. Carbon monoxide is a product of incomplete combustion and also is produced within the atmosphere by the oxidation of volatile organic compounds. The lifetime of carbon monoxide varies as a function of season and latitude but is on the order of months [Talbot *et al.*, 1996]. Carbon monoxide has a relatively simple and well-understood chemistry and better documented, but still rather uncertain, direct sources than most shorter-lived species. Therefore it is a good species with which to evaluate the chemical and transport characteristics of tracer models [Kanakidou *et al.*, 1999].

[6] The intercomparison has two major objectives. First, we statistically analyze the aircraft-derived and seven numerically derived versions of CO. These CTM simulations were prepared following the field phase of TRACE-P using a common set of emissions. The resulting statistics document the overall ability of the CTMs to simulate CO. The analyses examine plumes of CO, focusing on their concentrations, as well as their horizontal placements, altitudes, and depths. Next, we identify and draw attention to the key meteorological processes that influence CTM performance. We focus on how differing parameterizations related to boundary layer processes and deep convection affect each model's CO simulations. Our intent is to compare each model's simulations with the others and with observations, looking for similarities and differences, and searching for possible explanations.

2. Data and Methodologies

2.1. Chemical Transport Models

[7] Results from seven CTMs were examined in the study, three regional models and four global models. Details of each model are shown in Table 1, and a brief description of each model is given below.

2.1.1. FRSGC/UCI

[8] The Frontier Research System for Global Change/University of California, Irvine (FRSGC/UCI) global CTM [Wild and Prather, 2000] was run at T63 horizontal resolution ($1.9^\circ \times 1.9^\circ$) with 30 Eta levels in the vertical. For the current simulations it was driven by 3-hourly meteorological fields generated by the European Centre for Medium Range Weather Forecasts (ECMWF) Integrated Forecast System [Wild *et al.*, 2003]. Convective mass flux, cloud cover, precipitation and boundary layer height were supplied by the meteorological fields. Advection was calculated using the Prather scheme that conserves second-order moments [Prather, 1986]. Turbulent mixing was simulated by simple bulk mixing of the boundary layer at each model

step. The model uses the ASAD package for gas-phase tropospheric chemistry [Carver *et al.*, 1997], supplemented by a hydrocarbon oxidation scheme and a simplified treatment of stratospheric chemistry using the Linoz approach [McLinden *et al.*, 2000].

2.1.2. GEOS-CHEM

[9] The Goddard Earth Observing System-Chemistry model of tropospheric chemistry (GEOS-CHEM) global CTM [Bey *et al.*, 2001; Martin *et al.*, 2003] was run at a horizontal resolution of $2.0^\circ \times 2.5^\circ$ with 48 sigma levels in the vertical. It was driven by GEOS-3 assimilated meteorological data from the NASA Data Assimilation Office. The 3-D meteorological data were updated every 6 hours, while mixing depths and surface fields were updated every 3 hours. Advection was calculated using a semi-Lagrangian scheme [Lin and Rood, 1996]. Moist convection was computed using GEOS data for convective, entrainment, and detrainment mass fluxes [Allen *et al.*, 1996b]. In the current study, GEOS-CHEM was used in an offline chemistry mode. Loss of CO was computed using archived monthly mean fields of OH concentrations from a full-chemistry simulation [Martin *et al.*, 2003].

2.1.3. Meso-NH

[10] The Meso-NH regional nonhydrostatic mesoscale meteorological model [Lafore *et al.*, 1998; Mari *et al.*, 1999; Suhre *et al.*, 2000; Tulet *et al.*, 2003] was run at a horizontal resolution of 75×75 km with 72 pressure levels in the vertical. The vertical resolution was 50 m in the boundary layer and 400 m above the boundary layer up to 20 km. Boundary layer height was calculated as the altitude of the near surface layer having turbulent kinetic energy greater than $0.25 \text{ m}^2 \text{ s}^{-2}$. The boundary layer height was restricted to the first 3500 m to avoid turbulence from clouds. The domain was 0.76° – 59.3° N and 59° – 180° E. The dynamical time step was 60 s. Large-scale forcing of dynamical parameters was provided by ECMWF analyses at 6 hourly intervals. Convective mass flux was calculated within a convective mass transport algorithm. A CO tracer was introduced into the model to simulate the long-range transport of pollution. The tracer had the same primary source as carbon monoxide but had no indirect sources from the oxidation of methane or non-methane hydrocarbons. This tracer was coupled online with the model's transport (advection, convection, turbulent mixing). Initial and boundary conditions of CO were provided by GEOS-CHEM at six hourly intervals. [Bey *et al.*, 2001].

2.1.4. RAQMS-Global

[11] The Regional Air Quality Modeling System (RAQMS) global meteorological and chemical model was run at a horizontal resolution of $2.0^\circ \times 2.0^\circ$ with 12 Eta layers in the vertical from the surface to 336 K, then 14 isentropic layers up to 3300 K. Simulations were conducted online using instantaneous meteorological conditions from the University of Wisconsin-Madison (UW) hybrid model [Pierce *et al.*, 1991; Zapotocny *et al.*, 1994]. The RAQMS-Global model was initialized on 15 February 2001 using ECMWF analyses and a February monthly mean chemical distribution from a multiyear climate simulation from the NASA Langley Research Center (LaRC) Interactive Modeling Project for Atmospheric Chemistry and Transport (IMPACT) model [Pierce *et al.*, 2000; Al-Saadi *et al.*, 2001]. The IMPACT

Table 1. Descriptions of the Seven CTMs That Were Investigated in the Study

Institutions:	FRSGC/UCI	GEOS-CHEM v4.20	RAQMS-Global	UMD CTM	Meso-NH v4.3.1	RAQMS-Regional	STEM v. Y2K1
Frontier Research System for Global Change	Harvard University/ NASA Data Assimilation Office	http://www-as.harvard.edu/chemistry/trop/geos	NASA LaRC and University of Wisconsin	University of Maryland	Meteo-France/Laboratoire d'Aerologie	NASA LaRC and University of Wisconsin	Center for Global Environmental Research (CGRER), University of Iowa
Website:	http://www-as.harvard.edu/chemistry/trop/geos	http://www.ssec.wisc.edu/theta	http://rossby.larc.nasa.gov http://www.ssec.wisc.edu/theta	N/A	http://www.aero.obs-mjp.fr/mesonh/index2.html	http://rossby.larc.nasa.gov http://mocha.meteor.wisc.edu	http://www.cgrer.uiowa.edu/CTM_index.htm
Domain:	Global	Global	Global	Global	Regional	Regional	Regional
Meteorology:	GEOS-3 DAS	GEOS-3 DAS	UW hybrid model	GEOS-3 SG-DAS	ECMWF	UW-NMS	RAMS
Resolution	Temporal: 1 hour	Temporal: 900 s	Temporal: 1800 s	Temporal: 450 s	Temporal: 60 s	Temporal: 1800 s	Temporal: 10 min
	Horizontal: T63 (1.875 × 1.875 deg)	Horizontal: 2.0 × 2.5 deg	Horizontal: 2.0 × 2.0 deg	Horizontal: 0.5 × 0.5 deg	Horizontal: 75 km × 75 km	Horizontal: 110 km × 110 km	Horizontal: 80 km × 80 km
	Vertical: 30 Eta levels	Vertical: 48 Sigma levels	Vertical: 12 Eta levels and 14 isentropic levels	Vertical: 18 pressure levels	Vertical: 72 Z levels	Vertical: 50 Z levels	Vertical: 18 RAMS' sigma-z levels
Schemes:	Advection: Second-order moment scheme [Prather, 1986]	Advection: Semi-Lagrangian [Lin and Rood, 1996]	Advection: A flux piecewise parabolic method [Allen et al., 2000]	Advection: Nonuniform grid extension [Allen et al., 2000]	Advection: A flux-corrected transport scheme (FCT)	Advection: 6th order Crowley scheme in flux form	Advection: Upward Crank-Nicolson-Galerkin+Forester filtering or spectrally constrained cubics
	Turbulence: Assume full mixing within GEOS-diagnosed mixed layer generated by surface instability	Turbulence: Assume full mixing within GEOS-diagnosed mixed layer generated by surface instability	Turbulence: Nonlocal atmospheric boundary layer (Holtslag) and mass-flux convection [Zhang and McFarlane, 1995]	Turbulence: multidimensional and semi-Lagrangian extension of the piecewise parabolic method of [Colella and Woodward, 1984]	Turbulence: Quasi 1-D turbulence scheme of Bougeault and Lacarrere [1989]	Turbulence: Emanuel convection	Turbulence: ABL-scaling or Blackadar-mixing
	Resistances-in-series dry dep; rainout and washout based on solubilities	Deposition: N/A	Deposition: CCM3 Deposition: Species, surface type, and drag coefficient dependent	Deposition: method of [Colella and Woodward, 1984]	Deposition: "Big leaf" resistance model after [Walek, 1986] and [Wesley, 1989]	Deposition: Rainout based on fixed first-order pressure dependent rate constants	Deposition: "Big leaf" resistance model after [Walek, 1986] and [Wesley, 1989]
	Chemistry: ASAD package plus NMHC oxidation [Wild and Prather, 2000]	Chemistry: N/A	Chemistry: Standard stratospheric Ox-ClOx-BrOx-HOx-NOx cycles and oxidation of CH4 and CO to account for background tropospheric ozone production	Chemistry: N/A	Chemistry: No chemistry sink or source	Chemistry: Standard stratospheric Ox-ClOx-BrOx-HOx-NOx cycles and oxidation of CH4 and CO to account for background tropospheric ozone production	Chemistry: SAPRC99 mechanism [Carter et al., 2000] with second-order Rosenbrock solver [Perver et al., 1999], simplified liquid phase [Carmichael et al., 2003], and explicit online TUV calculation for photolysis rates
	Clouds: GEOS cloud mass fluxes <= 0, GEOS cloud fraction amounts. Moist convection computed using GEOS convective, entrainment, and detrainment mass fluxes [Allen et al., 1996a, 1996b]	Clouds: GEOS cloud mass fluxes <= 0, GEOS cloud fraction amounts. Moist convection computed using GEOS convective, entrainment, and detrainment mass fluxes [Allen et al., 1996a, 1996b]	Clouds: GEOS cloud mass fluxes and detrainment from GEOS-DAS rates	Clouds: OH fields from [Spivakovsky et al., 2000]	Clouds: Transport by subgrid wet convective updrafts and downdrafts is applied within the convective mass transport algorithm	Clouds: Constant 30% cloud albedo for stratospheric photolysis rates. Clear sky (10% albedo) for tropospheric photolysis rates	Clouds: Online calculation of photolysis; vertical transport calculated using enhanced diffusivity diagnosed from cloud bottom and top

climate simulation used the TRACE-P CO emission data set. Meteorological forecasts were reinitialized every 6 hours using ECMWF analysis. Convective mass flux, cloud cover, precipitation, and boundary layer height were supplied by the meteorological fields. The RAQMS-Global chemical predictions spanned the entire TRACE-P period. Advection was calculated using a flux form piecewise parabolic method. RAQMS includes standard stratospheric Ox-CIOx-BrOx-HOx-NOx cycles and oxidation of CH₄ and CO to account for background tropospheric ozone production.

2.1.5. RAQMS-Regional

[12] The Regional Air Quality Modeling System (RAQMS) regional meteorological and chemical model was run at a horizontal resolution of 110 × 110 km, with 50 vertical levels. The domain was 2°–48°N and 76°–154°E, and the dynamical time step was 2 min. Calculations were conducted online using instantaneous meteorological conditions from the UW Non-hydrostatic Modeling System (UW-NMS) [Tripoli, 1997]. ECMWF analyses were used for meteorological boundary conditions and to initialize the UW-NMS. Advection was calculated using a 6th order Crowler scheme in flux form. The RAQMS chemical module was the IMPACT model described above [Pierce et al., 2000; Al-Saadi et al., 2001]. Initial and boundary conditions of CO were provided by RAQMS-Global at six hourly intervals.

2.1.6. STEM

[13] The Sulfur Transport Eulerian Model (STEM) regional CTM [Carmichael et al., 1986, 1990] was run at a horizontal resolution of 80 × 80 km, with 18 vertical levels defined in the Regional Atmospheric Modeling System's (RAMS) sigma-z coordinate system. The domain was 8°–53°N and 75°–163°E, and the dynamical time step was 10 min. Large-scale forcing of dynamical parameters was provided by RAMS driven by 6 hourly ECMWF reanalysis data. Advection was calculated using the Galerkin scheme [McRae et al., 1982]. Convective mass flux, cloud cover, precipitation, and boundary layer height were supplied by the meteorological fields, while convective and vertical diffusion were computed using a simple K scheme. STEM employs a chemical mechanism tool, the kinetic preprocessor for chemical mechanism (KPP), to determine the chemical reactions. For the current simulations STEM used the SAPRC99 chemical mechanism [Carter, 2000] and the second-order Rosenbrock method [Verwer et al., 1999]. Initial and boundary conditions of CO were specified by fixed vertical profiles. The lateral boundary condition (LBC) was based on TRACE-P P3-B Flight 11 which flew over the South China Sea. This flight's CO profile was thought to best represent background values over water. The LBC varied vertically, but not horizontally. The LBC over land was obtained by adding 40 ppbv to the CO profile over water. This technique is based on experimental results. India and Russia are the primary inflow LBC for southern and northern portions of the TRACE-P domain, respectively. Characteristics of Indian outflow are described by De Gouw et al. [2001]. For the northern LBC, only measurements from surface stations were available. Pochanart et al. [2003] discuss the Siberian air mass and European inflow.

2.1.7. UMD CTM

[14] A stretched-grid version of The University of Maryland Chemistry and Transport Model (UMD CTM) [Allen et

al., 2000] was run on a horizontal grid with 0.5° × 0.5° resolution in the region of interest (10°–40°N; 100°–150°E), stretching to 2.2° (in longitude) × 1.9° (in latitude) on the opposite side of the globe, with 17 sigma and 18 pressure levels in the vertical. The model was driven by 6 hourly meteorological fields from version 3 of the Goddard Earth Observing System Stretched-Grid Data Assimilation System (GEOS-3 SG-DAS) [Fox-Rabinovitz et al., 2002]. Planetary boundary layer depth, upward cloud mass flux and detrainment were supplied by the meteorological fields. Advection was calculated using a nonuniform grid version [Allen et al., 2000] of Lin and Rood's [1996] multidimensional and semi-Lagrangian extension of the piecewise parabolic method [Colella and Woodward, 1984]. Vertical transport of trace gases by deep convection was parameterized using cumulus mass flux and detrainment profiles from GEOS-3 SG-DAS [Allen et al., 1996b]. Since convection in the GEOS-3 SG-DAS is performed on a uniform 1° × 1° grid, these fields were interpolated onto the stretched-grid before use. Turbulent mixing was calculated through a fractional mixing scheme [Allen et al., 1996a] in which complete mixing of the boundary layer is assumed. Chemical production and loss of CO were prescribed in a manner similar to that of Allen et al. [1996b] (i.e., prescribed OH concentrations [Spivakovsky et al., 2000] are used for computing CO loss and CO production from CH₄). Carbon monoxide yields from oxidation of nonmethane hydrocarbons were prescribed as in the work of Allen et al. [1996b].

2.2. Emissions Data

[15] The special simulations reported here were prepared after the field phase of TRACE-P was completed, i.e., they are not the simulations used during real time flight planning. Five of the seven CTMs used the same initial CO distributions on the first date of their TRACE-P simulation, 15 February 2001. This common initial CO field was prepared at Harvard University using GEOS-CHEM [Bey et al., 2001]. Both RAQMS model simulations did not use these initial conditions. Instead, they used the February monthly mean chemistry from the IMPACT model to initialize the global chemistry on 15 February.

[16] Each of the seven models used the same CO emissions data during their simulations. These emissions are the only consistent variable among the models. This choice was influenced by Kanakidou et al.'s [1999] conclusion that “in future intercomparison exercises, models should preferably use the same emission inventories as input, thereby ruling out differences between inventories as a cause of differences between models.” However, it should be noted that indirect sources of CO (i.e., oxidation of hydrocarbons) also contributed to the CO budget during the TRACE-P period. These sources are treated differently in the seven different models (see section 2.1 and Table 1). For example, Mesonh and RAQMS did not include nonmethane hydrocarbon (NMHC) oxidation in their simulations. Fortunately, spatial and temporal variations of “oxidation-produced” CO in the TRACE-P region are much smaller than variations in “directly emitted” CO.

[17] The global 1° × 1° emissions fields were created at Harvard University, consisting of Streets' Asian emissions [Streets et al., 2003; Woo et al., 2003] superimposed on Logan's global emissions [Duncan et al., 2003; Yevich and

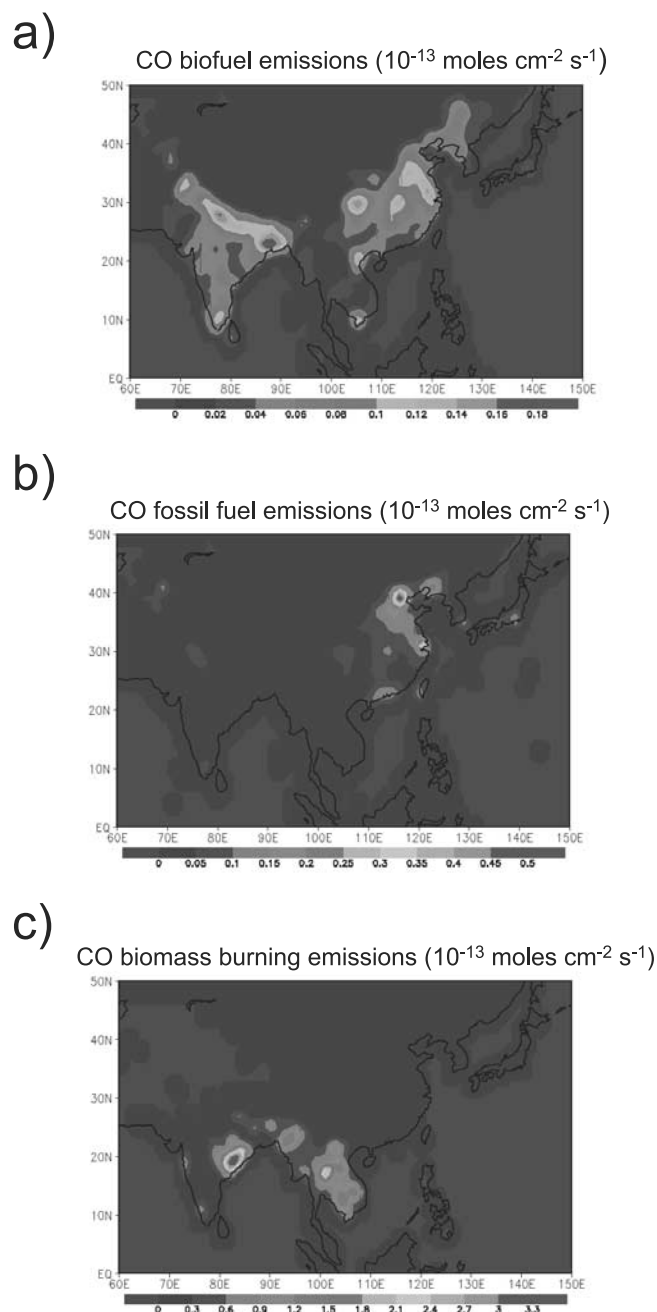


Figure 1. CO emissions used by all CTMs in this study from (a) biofuels, (b) fossil fuels, and (c) biomass burning. See color version of this figure at back of this issue.

Logan, 2003]. Figures 1a, 1b, and 1c show the distribution of Asian CO emissions during the TRACE-P period from biofuel, fossil fuel, and biomass burning, respectively. Anthropogenic emissions include fuel combustion (fossil and wood) and industrial activities. Biomass burning emissions include sources from forest wildfires, deforestation, savanna burning, slash-and-burn agriculture, and agricultural waste burning.

[18] Logan's global emissions represent 1985 values [Duncan *et al.*, 2003; Yevich and Logan, 2003]; however, the fossil fuel emissions subsequently were scaled to 1998 values. The 1985 and 1998 values are similar because a

decrease in European emissions is offset by an increase in Asian emissions. These scaled 1998 values were estimated using different methods for various regions of the world. In Europe and Canada, CO estimates prepared by the Co-operative Programme for Monitoring and Evaluation of the Long-Range Transmission of Air Pollutants in Europe (EMEP) were used [EMEP, 1998]. Estimates by the Organisation for Economic Co-operation and Development (OECD) were used in Japan [OECD, 1997]; Environmental Protection Agency (EPA) estimates were used in the United States [EPA, 1997]; and for the rest of the world, a relationship between fossil fuel CO and liquid CO₂ usage was used to scale the CO emissions (Andrew Fusco, Harvard University, personal communication, year?). CO₂ statistics were taken from the Carbon Dioxide Information Analysis Center (CDIAC) [Marland *et al.*, 1999]. Biofuel and fossil fuel emissions represent yearly averages, while biomass burning emissions vary monthly.

[19] Streets' Asian emissions represent 2000 values [Streets *et al.*, 2003; Woo *et al.*, 2003]. His fossil fuel CO emissions include domestic fossil fuel, large point sources, industry, and transport, while his biofuel CO emissions include domestic biofuel. Biomass burning emissions were not provided by Streets. The CO global emissions used in this study are given in Table 2.

2.3. Model Output

[20] As described above, each of the six modeling groups produced special simulations for the intercomparison, using the same common set of emissions data. Results of the postmission simulations were sent to the intercomparison coordinators at Florida State University (FSU). Modelers did not revise their submitted results after the second TRACE-P data workshop during June 2002, except for correcting errors in input conditions and output diagnostics.

[21] Each modeling group provided several types of results to the FSU coordinators. One set of simulated CO data was interpolated to the latitude, longitude, pressure, and time of specified locations along each of the DC-8 flight tracks shown in the work of Jacob *et al.* [2003]. These locations correspond to those of a merged chemical data set (see section 2.4) prepared at NASA Langley Research Center (LaRC) and to sets of backward air trajectories prepared at FSU [Fuelberg *et al.*, 2003]. These simulated CO flight track data are compared with observed aircraft-derived CO in the following sections.

[22] Three-dimensional model-derived CO data at 6 hourly intervals also were provided throughout the entire TRACE-P period. The domain of these data for the global CTMs was 0°–120°W and 10°S–80°N or was the full domain for each of the regional models. This large area allowed us to examine the evolution of CO plumes as far back as Europe. The three-dimensional data were examined during selected flights in which the origins and evolutions of plumes were influenced

Table 2. Global CO Budget Used in Simulations^a

	Logan [1985]	Logan [1998]	Logan [1998] + Streets
Fossil fuel emissions	391.5	394.0	318.4
Biofuel emissions	159.4	159.4	168.4
Biomass burning emissions	436.9	436.9	436.9

^aValues are annual means in Tg CO yr⁻¹. See text for details.

greatly by meteorological processes such as boundary layer emissions, deep convection, or frontal processes. The data permitted examination of major CO plumes, focusing on their concentrations as well as their horizontal placements, altitudes, and depths.

[23] Finally, most modeling groups provided four parameters describing boundary layer processes and deep convection, i.e., boundary layer depth, cloud top height, convective mass flux and detrainment. These data were compared with satellite imagery, rainfall estimates, and lightning data. They also were used to isolate differences among the models.

[24] Backward air trajectories were calculated at FSU using 6 hourly ECMWF global reanalyses as described by *Fuelberg et al.* [2003]. These global data do not adequately describe small-scale processes such as individual convective updrafts and downdrafts but only include their parameterized effects. Trajectory locations correspond to those in the merged data set described in the next section. Thus the trajectories could be used to identify source regions of the air samples to describe mechanisms responsible for transporting the chemical species along the flight tracks.

2.4. Observational Data

[25] An extensive set of in situ chemical data was collected during the TRACE-P campaign by the different investigators. Sampling frequencies varied from 1 s for CO measurements to over 1200 s for other species. *Jacob et al.* [2003] discuss the various species sampled by the investigators, including the techniques used to make the measurements and the limits of detection (LOD) for each instrument. Of particular interest to the current study, *Sachse et al.* [1987] describe the measurement of CO using a spectrometer system called "DACOM" (Differential Absorption CO Measurement) which includes three tunable diode lasers providing radiation data at 4.7, 4.5, and 3.3 μm , corresponding to the absorption lines for CO, N₂O, and CH₄, respectively.

[26] A merged chemical data set prepared at NASA LaRC links the in situ chemical data with the various sets of trajectories. The merge was calculated at 5 min intervals along horizontal portions of flight tracks and at 25 hPa intervals during ascents and descents.

3. Statistical Analysis

3.1. Combined Flights

[27] Figure 2 shows scatterplots of modeled versus aircraft-derived CO for the combination of DC-8 flights 7–17, the flights simulated by each of the seven models. A total of 3554 points comprise each panel. Linear least squares fits of the data (solid line) and 1 to 1 lines (dashed) are shown for each plot. Table 3a shows the mean difference between simulated and model-derived CO (ppbv), root mean square (RMS) difference (ppbv), linear correlation, and slope of each model's simulation versus aircraft-derived CO for the combined 11 flights.

[28] Although the models produce varying results, there are common characteristics. Biases are most pronounced during large CO events. The mean difference exhibits a large variation between models (from -67 to $+15$ ppbv); however, the differences generally are negative. This negative bias could reflect an underestimate in the prescribed

CO sources. Using an emissions inventory similar to Logan's global data set developed at Harvard, *Bey et al.* [2001] noted that underestimates of observed CO concentrations could reflect a problem with current source inventories as well as an overestimate of OH.

[29] The models also have unique characteristics. RMS differences for individual models range from 70 to 94 ppbv. We will highlight possible causes for these large differences in later sections. Correlations for individual models range from 0.44 to 0.75, with most values between 0.55 and 0.65. Although linear slopes range from 0.16 to 0.62, most are on the lower end of this spectrum, indicating the differential bias noted earlier, i.e., larger values are most underestimated. Statistics from the four global models and three regional models do not differ greatly, suggesting that increased model resolution does not necessarily produce better statistics with respect to measurements.

[30] It must be noted that the STEM regional model used fixed vertical profiles as boundary conditions (section 2.2), while Meso-NH and RAQMS-Regional used global model forecasts for boundary conditions. STEM's boundary condition CO concentrations are greater than those from the prescribed global emission fields. This is believed to be the reason why STEM does not have a negative bias. One also should note that Meso-NH and RAQMS did not include NMHC oxidation, which is thought to explain a portion of these models' large negative biases.

3.2. Individual Flights

[31] The models' statistical agreements vary greatly among the individual flights (Table 4). Considering all models and flights, mean differences range from -91 to $+52$ ppbv; RMS differences range from 16 to 146 ppbv, and correlations range from 0.00 to 0.92. However, for each given flight, the models generally produce similar relative statistical results. Most correlations for flights 8, 11, 12 and 13 are within ± 0.30 of each other. For example, the various correlations for flight 8 range from 0.51 to 0.84. Conversely, for flights 7, 9, 10, 14, 15, 16 and 17 a single model exhibits large discrepancies compared to the other six models. For example, Meso-NH correlations are smaller than the six other models for flights 9, 15 and 17. UMD CTM has the greatest correlation for flights 14 and 17 but the smallest for flight 10. RAQMS-Regional has the smallest correlation for flight 14 but the largest for flight 15. These nonregular discrepancies suggest that there is not a systematic error in the models. Instead, the individual smaller correlations most likely are caused by the displacement of, or inaccurate representation of concentrations within a particular plume or lamina in a model.

[32] We selected three flights to describe in detail. Figure 3 shows their time series. Each time series includes aircraft altitude, aircraft-derived CO, and the seven model-derived simulations.

[33] DC-8 flight 8 (Hong Kong Local 2) is illustrated because its seven simulations are consistently among the best (Figure 3a). Most models produce RMS differences near 40 ppbv and correlations near 0.80 (Table 4). The models are most consistent in areas of relatively small CO. Although each model produces a noticeable response in areas of enhanced observed CO, the intensity of that response varies greatly. For example, measured CO at

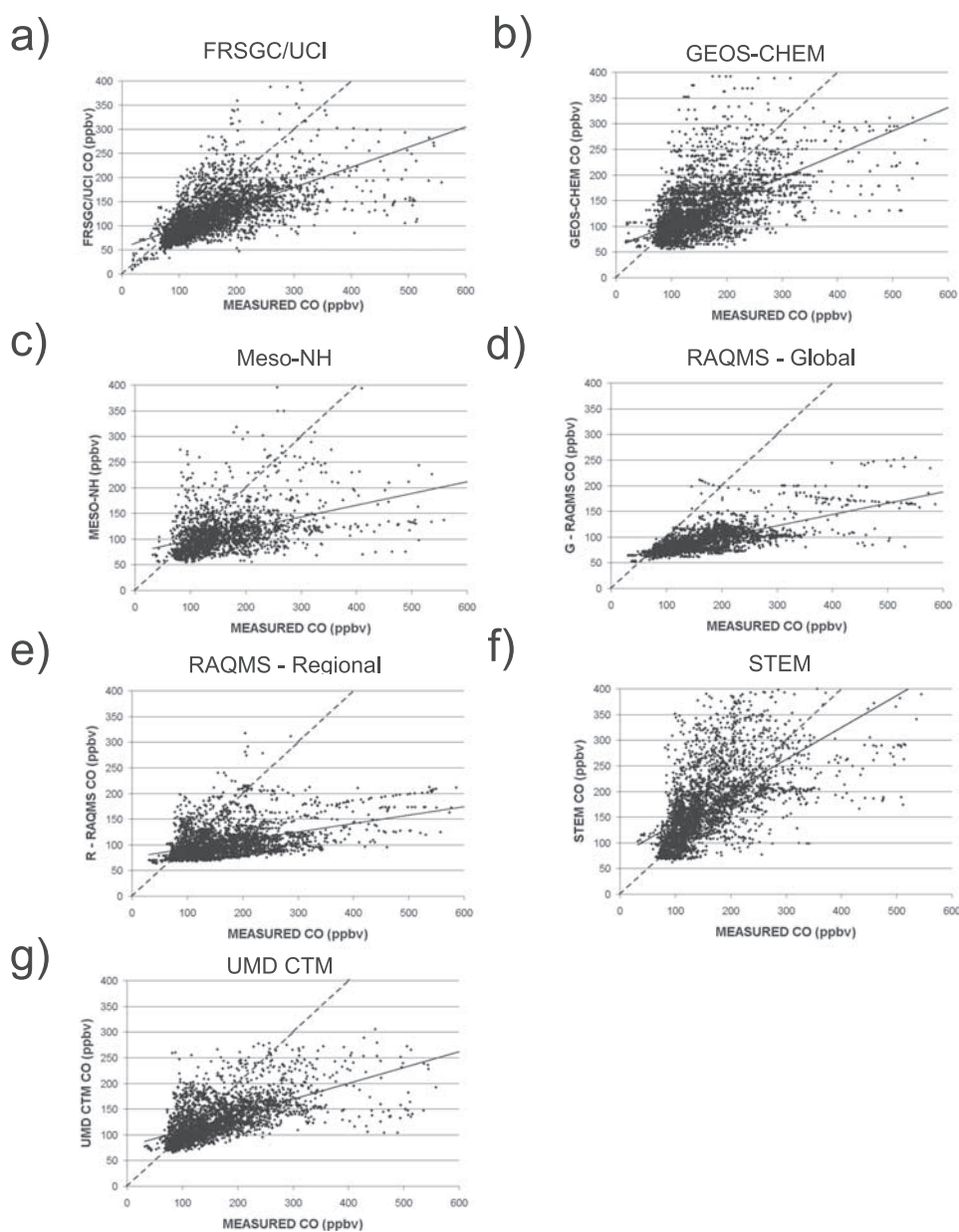


Figure 2. Scatterplots of modeled versus aircraft-derived CO for the combination of DC-8 flights 7–17; (a) FRSGC/UCI, (b) GEOS-CHEM, (c) Meso-NH, (d) STEM, (e) RAQMS-Global, (f) RAQMS-Regional, and (g) UMD CTM. Linear least squares fits of the data (solid line) and 1 to 1 lines (dashed) are shown in each plot. Statistics for each panel are given in Table 3.

0300 UTC is 216 ppbv, while simulated CO values interpolated to that exact location vary from STEM's value of 255 ppbv to RAQMS-Regional's result of 101 ppbv. However, most models produce better results for the CO spikes at times slightly earlier or later than the observed time, suggesting a misplacement of the model-derived plume. This aspect is investigated in section 4.3. The rather small fluctuations of CO during this flight are thought to be the reason why its model simulations are consistently among the best.

[34] DC-8 flight 10 (Hong Kong Local 4) exhibits some of the greatest discrepancies among the models (Figure 3b). The time series and statistics (Table 4) show that most of the

models perform poorly during this flight, with correlations ranging from 0.13 to 0.71. The UMD CTM has the smallest correlation, but it exhibits nearly the best mean difference (−10 ppbv) and RMS difference (53 ppbv). The small correlation produced by the UMD CTM (0.13) occurs because the model incorrectly predicts that a 0730 UTC boundary layer plume has lower mixing ratios than a 0850 UTC midtropospheric plume. STEM produces the best correlation (0.71). STEM simulates enhanced regions of CO well, but its values are too small during flight legs of relatively constant CO. The large fluctuations of CO during this flight are believed to be the cause of inconsistency among model simulations.

Table 3. Mean Difference of CO, RMS Difference, Correlation, and Slope for the Combination of DC-8 Flights 7–17, Those Portions of DC-8 Flights 7–17 That Meet the Criteria of a Plume, and Those Portions of DC-8 Flights 7–17 With the Plume Events Removed^a

Model	Mean Difference	RMS Difference	Correlation	Slope
<i>All Cases</i>				
FRSGC/UCI	-36.9	70.1	0.65	0.37x + 64.5
GEOS-CHEM	-20.6	69.5	0.56	0.41x + 73.5
Meso-NH	-49.7	87.1	0.44	0.23x + 74.2
RAQMS-Global	-67.3	94.4	0.75	0.22x + 55.4
RAQMS-Regional	-56.3	91.4	0.48	0.16x + 75.3
STEM	14.6	70.6	0.61	0.62x + 75.4
UMD CTM	-34.3	70.9	0.62	0.31x + 77.1
<i>Plumes</i>				
FRSGC/UCI	-193.3	220.4	0.10	0.06x + 165.9
GEOS-CHEM	-168.2	199.1	0.21	0.16x + 151.9
Meso-NH	-230.8	256.8	0.07	0.05x + 139.1
RAQMS-Global	-289.7	315.6	0.23	0.03x + 108.8
RAQMS-Regional	-256.6	290.3	0.43	0.12x + 94.1
STEM	-112.9	154.5	0.33	0.31x + 153.1
UMD CTM	-220.3	223.1	0.16	0.08x + 152.4
<i>Plumes Removed</i>				
FRSGC/UCI	-22.8	41.9	0.67	0.55x + 40.0
GEOS-CHEM	-7.8	49.3	0.50	0.56x + 53.6
Meso-NH	-33.7	57.3	0.37	0.28x + 67.3
RAQMS-Global	-45.2	63.3	0.36	0.09x + 79.4
RAQMS-Regional	-37.0	57.5	0.37	0.21x + 71.1
STEM	14.5	48.0	0.66	0.87x + 32.0
UMD CTM	-19.7	43.9	0.55	0.40x + 64.2

^aUnits for mean difference and RMS difference are ppbv. See text for details.

[35] The various models also do a good job of simulating CO during most of DC-8 flight 13 (Yokota Local 1) (Figure 3c). This flight traveled over the Yellow Sea, recording the largest CO concentrations during TRACE-P (approximately 1200 ppbv). Although each model correctly locates the intense Shanghai plume that was sampled on two flight legs (near 0450 and 0600 UTC), each model greatly underestimates its intensity. For example, the measured CO at 0445 UTC is 966 ppbv, while the greatest simulated CO varies from STEM's value of 383 ppbv to Meso-NH's result of 142 ppbv. Inadequate simulation of these major plumes causes mean differences (-73 to +18 ppbv) and RMS differences (94 to 146 ppbv) for flight 13 to be among the worst of the eleven flights (Table 4).

3.3. Plumes

[36] The models' difficulties in simulating the intense plumes during DC-8 flight 13 prompted us to investigate this issue further. We examined all regions of enhanced CO to understand better the differences between model simulations and observations. We defined a "plume" using the criterion that the sampled air must exhibit CO values that are enhanced at least 20 ppbv above the local background. The local background was defined as the average of all CO measurements within a layer. For this purpose, we divided the atmosphere into five layers (below 850 hPa, 850–700 hPa, 700–500 hPa, 500–300 hPa, 300 hPa and above), giving each flight five unique local background values. This classification is based on procedures defined by Mauzerall *et al.* [1998]. Table 3b shows statistics for those segments of

Table 4. Mean Difference of CO, RMS Difference, Correlation, and Slope for Individual DC-8 Flights 7–17^a

Model	Mean Difference	RMS Difference	Correlation	Slope
<i>Flight 7</i>				
FRSGC/UCI	-40.6	78.1	0.69	0.47x + 43.1
GEOS-CHEM	-11.9	77.8	0.63	0.59x + 52.3
Meso-NH	-11.9	74.7	0.65	0.52x + 64.1
RAQMS-Global	-49.4	87.4	0.31	0.05x + 92.5
RAQMS-Regional	-51.3	87.9	0.39	0.06x + 89.1
STEM	1.3	83.5	0.59	0.59x + 66.6
UMD CTM	-18.9	68.7	0.69	0.45x + 68.3
<i>Flight 8</i>				
FRSGC/UCI	-25.5	40.7	0.84	0.60x + 27.9
GEOS-CHEM	-25.4	43.5	0.79	0.69x + 14.4
Meso-NH	-30.4	52.2	0.65	0.35x + 54.1
RAQMS-Global	-28.3	58.4	0.51	0.13x + 76.1
RAQMS-Regional	-36.3	64.3	0.82	0.14x + 70.5
STEM	2.8	40.8	0.84	1.10x - 39.9
UMD CTM	-23.9	40.8	0.84	0.51x + 39.9
<i>Flight 9</i>				
FRSGC/UCI	-32.2	69.7	0.58	0.35x + 81.5
GEOS-CHEM	-15.6	69.9	0.53	0.44x + 81.6
Meso-NH	-46.8	92.5	0.28	0.16x + 100.6
RAQMS-Global	-80.1	111.1	0.74	0.13x + 78.1
RAQMS-Regional	-72.4	106.2	0.52	0.14x + 83.2
STEM	4.3	76.2	0.44	0.39x + 110.5
UMD CTM	-34.8	70.6	0.59	0.30x + 86.7
<i>Flight 10</i>				
FRSGC/UCI	-24.1	41.8	0.67	0.43x + 55.3
GEOS-CHEM	-3.1	42.5	0.47	0.36x + 86.3
Meso-NH	-39.4	58.9	0.35	0.18x + 74.1
RAQMS-Global	-40.7	52.3	0.43	0.09x + 84.4
RAQMS-Regional	-47.1	54.8	0.63	0.31x + 48.7
STEM	4.5	41.0	0.71	0.89x + 20.5
UMD CTM	-9.7	52.9	0.13	0.09x + 118.5
<i>Flight 11</i>				
FRSGC/UCI	-28.9	59.5	0.53	0.33x + 68.6
GEOS-CHEM	-2.1	57.3	0.51	0.46x + 77.1
Meso-NH	-33.4	16.2	0.61	0.30x + 69.9
RAQMS-Global	-46.4	73.1	0.42	0.09x + 80.6
RAQMS-Regional	-28.6	63.6	0.43	0.29x + 69.7
STEM	22.3	54.0	0.74	0.89x + 38.7
UMD CTM	-21.1	60.7	0.68	0.39x + 67.7
<i>Flight 12</i>				
FRSGC/UCI	-35.4	77.4	0.75	0.39x + 67.8
GEOS-CHEM	22.9	89.5	0.54	0.43x + 120.1
Meso-NH	-56.8	97.2	0.63	0.25x + 66.7
RAQMS-Global	-60.8	114.7	0.53	0.09x + 90.5
RAQMS-Regional	-35.8	95.3	0.58	0.23x + 92.9
STEM	51.8	96.8	0.72	0.84x + 79.1
UMD CTM	-31.3	83.7	0.63	0.32x + 83.7
<i>Flight 13</i>				
FRSGC/UCI	-46.5	111.3	0.58	0.22x + 80.5
GEOS-CHEM	-31.4	101.7	0.63	0.26x + 87.9
Meso-NH	-65.5	127.6	0.51	0.12x + 77.8
RAQMS-Global	-73.1	145.5	0.75	0.07x + 74.2
RAQMS-Regional	-61.3	132.9	0.67	0.14x + 75.0
STEM	17.7	93.5	0.65	0.49x + 99.6
UMD CTM	-49.9	111.1	0.74	0.19x + 80.8
<i>Flight 14</i>				
FRSGC/UCI	-29.5	56.8	0.41	0.34x + 69.8
GEOS-CHEM	-31.1	50.3	0.56	0.37x + 63.6
Meso-NH	-57.8	70.1	0.63	0.29x + 49.9
RAQMS-Global	-68.6	78.6	0.51	0.07x + 76.3
RAQMS-Regional	-65.5	78.1	0.10	0.04x + 89.4
STEM	48.0	78.2	0.46	0.66x + 99.7

Table 4. (continued)

Model	Mean Difference	RMS Difference	Correlation	Slope
UMD CTM	-37.3	51.6	0.71	0.32x + 64.6
<i>Flight 15</i>				
FRSGC/UCI	-39.2	67.5	0.53	0.28x + 90.1
GEOS-CHEM	-33.6	77.9	0.25	0.12x + 123.3
Meso-NH	-61.4	93.6	0.00	0.00x + 115.2
RAQMS-Global	-78.1	86.6	0.51	0.09x + 76.2
RAQMS-Regional	-60.0	74.7	0.54	0.26x + 61.1
STEM	24.7	77.9	0.40	0.43x + 126.8
UMD CTM	-42.3	75.4	0.31	0.12x + 114.6
<i>Flight 16</i>				
FRSGC/UCI	-53.4	71.7	0.92	0.43x + 46.3
GEOS-CHEM	-42.6	62.7	0.89	0.48x + 48.3
Meso-NH	-73.3	102.7	0.46	0.16x + 78.2
RAQMS-Global	-73.1	101.6	0.61	0.10x + 74.9
RAQMS-Regional	-76.4	105.6	0.45	0.08x + 75.4
STEM	-7.6	55.5	0.80	0.37x + 102.8
UMD CTM	-56.5	79.2	0.87	0.32x + 61.3
<i>Flight 17</i>				
FRSGC/UCI	-53.7	63.9	0.81	0.44x + 53.7
GEOS-CHEM	-54.3	68.7	0.62	0.38x + 64.9
Meso-NH	-91.1	105.1	0.29	0.09x + 80.6
RAQMS-Global	-83.7	99.6	0.73	0.11x + 73.4
RAQMS-Regional	-84.7	99.5	0.71	0.15x + 66.3
STEM	-17.6	38.4	0.77	0.64x + 51.7
UMD CTM	-59.3	68.7	0.84	0.41x + 54.9

^aUnits for mean difference and RMS difference are ppbv.

DC-8 flights 7–17 meeting this definition. The results differ noticeably from those based on all measurements (Table 3a). For example, RMS differences frequently exceed 200 ppbv for the plumes, versus a range of 70 to 94 ppbv for all segments. All models produce plume correlations ≤ 0.43 , while they are ≤ 0.75 for the complete data set. Three of the model's plume correlations are ≤ 0.16 .

[37] It is clear that the models have great difficulty simulating the CO plumes. Two of the three regional models produce the greatest correlations (0.43 for RAQMS Regional and 0.33 for STEM), although their corresponding mean and RMS differences are not always among the best. For the global models, one might expect that those with coarser resolution would have the greatest difficulties reproducing the relatively small-scale plumes. However, Table 3b suggests that increased model resolution does not necessarily produce better statistics with respect to measurements. For example, the global model with the coarsest horizontal resolution, GEOS-CHEM, produces better results than some global models with finer resolution (e.g., FRSGC and UMD CTM). Discrepancies between simulated and measured plumes are due both to shifts in physical placement and differences in magnitude. Model simulations depend on emissions sources, internal chemistry, and resolution. These issues are discussed in section 4.3.

[38] To examine model simulations without the influence of major plumes, we removed those segments from each data set. Table 3c shows statistics for those portions of combined DC-8 flights 7–17 with the plumes removed. The statistics show that the models do a good job of simulating CO in this situation. Mean difference and RMS difference are smaller than those in Tables 3a and 3b, while the slopes

are greater. On the other hand, correlations generally do not improve.

3.4. Altitude Variations

[39] We investigated whether there was a relationship between CO error and altitude. For this purpose, we divided the atmosphere into five layers (below 850 hPa, 850–700 hPa, 700–500 hPa, 500–300 hPa, 300 hPa and above).

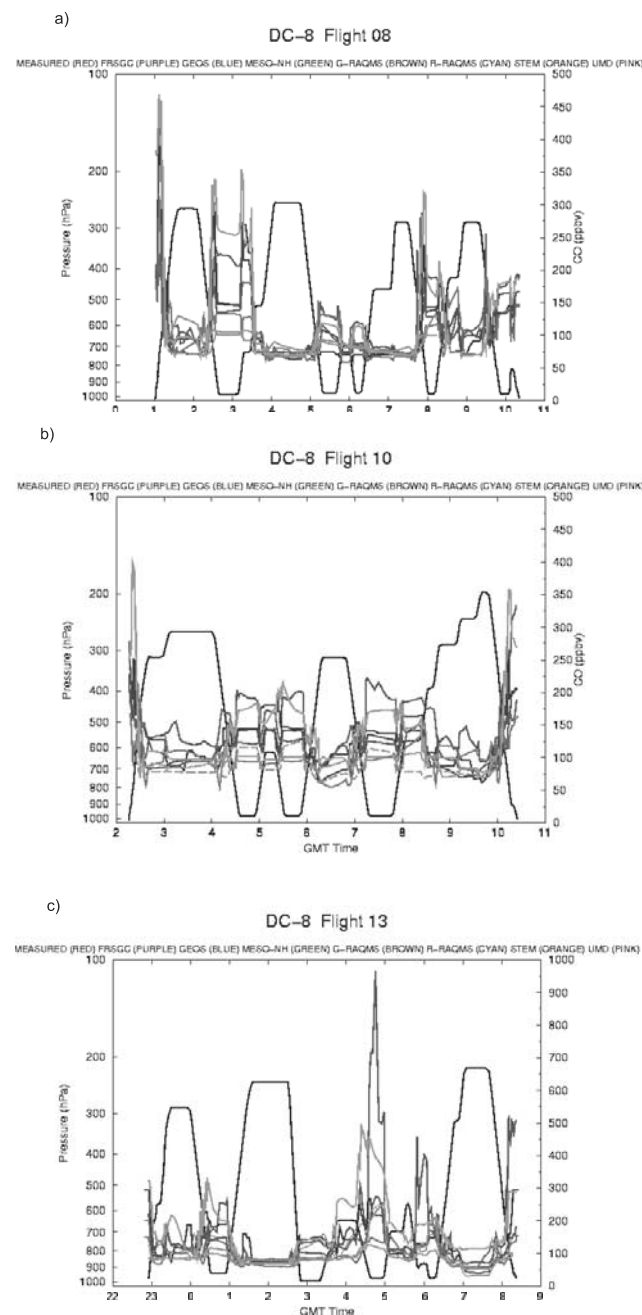


Figure 3. Time series of aircraft altitude (black), aircraft-derived CO (red), and the seven model-derived simulations for (a) DC-8 flight 8, (b) DC-8 flight 10, and (c) DC-8 flight 13. FRSGC/UCI (violet), GEOS-CHEM (blue), Meso-NH (green), RAQMS Global (brown), RAQMS Regional (cyan), STEM (orange), UMD CTM (pink). See color version of this figure at back of this issue.

Table 5. Mean Difference of CO, RMS Difference, Correlation, and Slope for Five Atmospheric Layers and the Entire Vertical Column for the Combination of DC-8 Flights 7–17

	FRSGC/UCI	GEOS-CHEM	Meso-NH	RAQMS-Global	RAQMS-Regional	STEM	UMD
<i>Mean Difference</i>							
Above 300 hPa	-14.7	-0.7	-13.5	-26.2	-12.5	-7.5	-6.4
500–300 hPa	-26.2	-12.9	-20.7	-35.8	-37.1	0.3	-6.3
700–500 hPa	-43.1	-20.3	-39.9	-51.7	-58.1	40.2	-20.2
850–700 hPa	-54.2	-36.8	-65.4	-80.7	-81.8	29.7	-47.6
Below 850 hPa	-47.1	-22.3	-99.5	-106.7	-121.8	-6.9	-81.4
All Levels	-36.9	-20.6	-49.7	-56.3	-61.8	14.6	-34.3
<i>RMS Difference</i>							
Above 300 hPa	38.6	45.5	31.6	47.1	38.8	41.5	31.2
500–300 hPa	53.2	52.5	49.5	67.1	61.9	48.1	41.3
700–500 hPa	75.5	75.4	74.4	78.0	78.1	75.1	51.7
850–700 hPa	87.2	82.7	99.7	108.0	101.7	82.6	78.3
Below 850 hPa	88.9	94.3	131.4	142.8	154.6	82.5	110.6
All Levels	70.1	69.5	87.1	91.4	96.3	70.8	71.1
<i>Correlation</i>							
Above 300 hPa	0.49	0.37	0.58	0.21	0.22	0.26	0.55
500–300 hPa	0.65	0.61	0.52	0.02	0.24	0.48	0.57
700–500 hPa	0.65	0.53	0.24	0.20	0.61	0.59	0.58
850–700 hPa	0.51	0.46	0.32	0.18	0.59	0.47	0.53
Below 850 hPa	0.59	0.45	0.45	0.47	0.64	0.52	0.65
All Levels	0.65	0.56	0.44	0.48	0.51	0.61	0.62
<i>Slope</i>							
Above 300 hPa	0.35x + 57.2	0.37x + 68.5	0.44x + 45.5	0.06x + 76.3	0.11x + 81.1	0.23x + 74.8	0.42x + 55.8
500–300 hPa	0.44x + 52.4	0.50x + 55.5	0.44x + 47.9	0.01x + 93.9	0.05x + 83.5	0.46x + 65.9	0.40x + 62.4
700–500 hPa	0.34x + 67.9	0.41x + 78.1	0.16x + 84.4	0.09x + 89.8	0.10x + 75.9	0.79x + 70.9	0.39x + 68.9
850–700 hPa	0.27x + 91.1	0.30x + 101.8	0.20x + 83.3	0.08x + 97.7	0.11x + 77.5	0.49x + 122.5	0.28x + 83.1
Below 850 hPa	0.31x + 85.3	0.31x + 110.9	0.16x + 89.6	0.14x + 88.8	0.09x + 81.8	0.40x + 127.3	0.24x + 89.1
All Levels	0.37x + 64.5	0.41x + 73.5	0.23x + 74.2	0.16x + 75.3	0.09x + 80.2	0.58x + 71.5	0.31x + 77.1

Table 5 shows statistics for these layers. The greatest mean differences (Table 5a) and RMS differences (Table 5b) occur in the lower levels. This is expected since many plumes are located relatively near the surface. It was shown earlier that the models have difficulties in these regions of enhanced CO. The correlations (Table 5c) show mixed results. Overall, the models tend to be less correlated with observations in the upper levels and moderately correlated with observations in the middle to lower levels. For example, the greatest correlations for the finer resolution models (RAQMS-Regional, STEM, UMD CTM), with the exception of Meso-NH, generally occur below 850 hPa. Each regional model, excluding Meso-NH, produces the worst correlations above 300 hPa. These small correlations could indicate that the regional models are unable to simulate the meteorological ascent that is needed to pump CO from its source regions at the surface to the upper levels. However, in general, statistics show that global CTMs present better correlations above 300 hPa than regional models. Therefore since CO at higher altitudes is more influenced by sources outside of the immediate TRACE-P region, this may cause difficulties for the regional CTMs. The unique behavior of Meso-NH is thought to result from its internal chemistry formulations, as discussed in section 2.1.

[40] We also examined very thin layers throughout the atmosphere (978–976 hPa, 908–906 hPa, 728–726 hPa, 606–604 hPa, 428–426 hPa and 328–326 hPa) to determine if part of the models' overall correlation (Table 3) was due to changes in altitude. These six layers were selected because they contained the greatest number of sampling points. The results (not shown) do not indicate large differences from the

correlations obtained over all levels (Table 3a). For example, correlations for GEOS-CHEM range from 0.40 to 0.83, versus a composite mean for all levels of 0.56. The best correlation (0.83) is at the 728–726 hPa level, and the worst (0.28) is for the 328–326 hPa level, similar to the findings for the deeper layers discussed above (Table 5). Similar results are observed for the other models.

4. Meteorological Processes

4.1. Composite Distributions

[41] Horizontal distributions of CO averaged over the TRACE-P period provide a useful intercomparison of model results. The models best agree on the placement and intensity of CO at low levels, i.e., close to the surface-based emission sources. Figure 4 compares spatial fields of CO at 850 hPa for the period 7–31 March, the dates encompassing DC-8 flights 7–17. The greatest model-derived CO is over eastern India, in the same region as strong biomass burning and biofuel emissions (Figure 1). There is a second area of enhanced simulated CO over Southeast Asia where strong biomass burning emissions are located. This pattern is similar at 700 hPa (not shown), although Meso-NH no longer shows the maximum over Southeast Asia. In the upper levels, e.g., at 300 hPa (Figure 5), all models show similar distributions, reflecting convective pumping over Southeast Asia, followed by long-range eastward transport over the Pacific. However, the overall intensity of CO varies widely among the models. The two CTMs using closely related meteorological input data, GEOS-CHEM and UMD CTM, exhibit very similar results, and generally produce

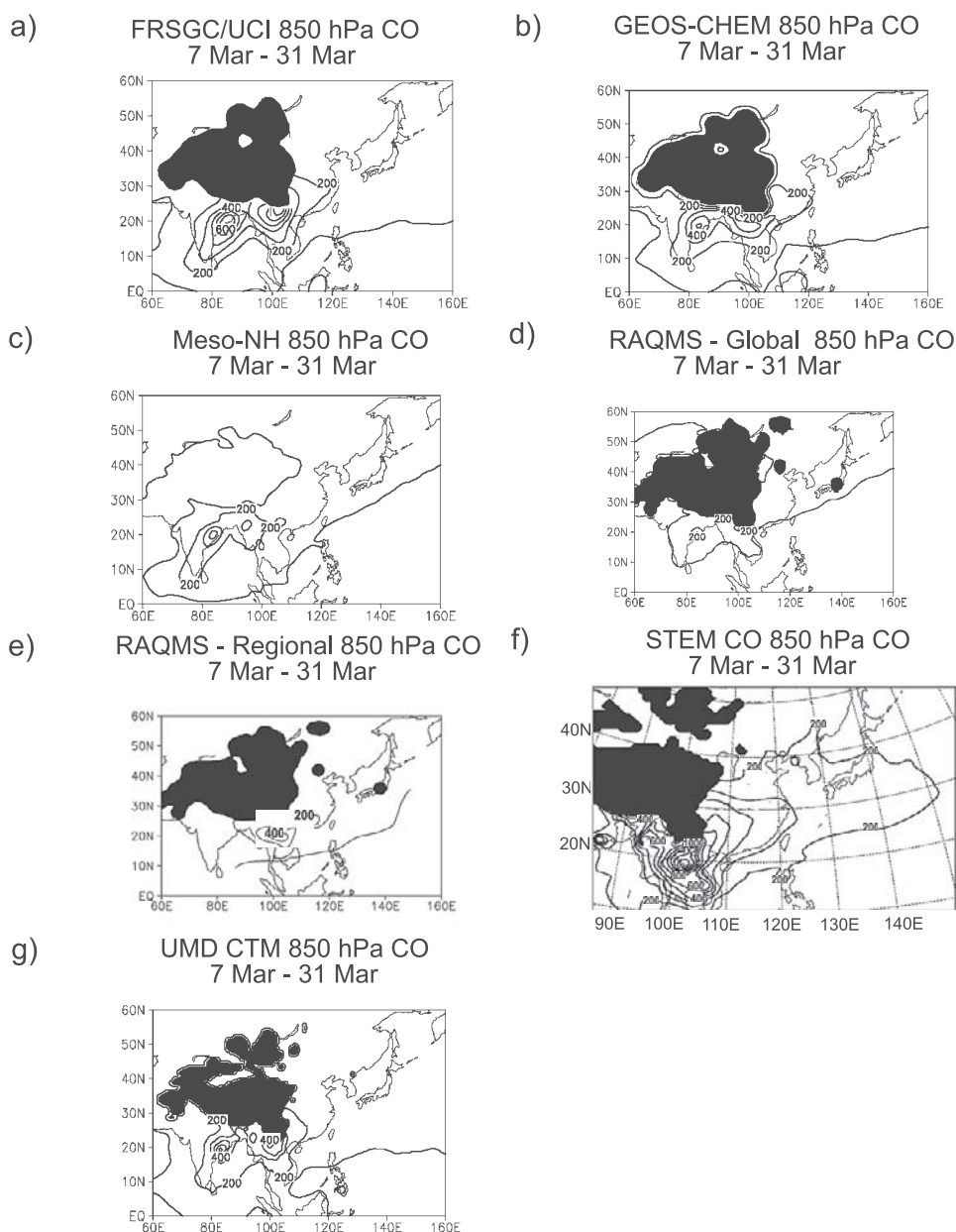


Figure 4. Spatial fields of model-derived CO (ppbv) at 850 hPa for the period 7–31 March. (a) FRSGC/UCI, (b) GEOS-CHEM, (c) Meso-NH, (d) RAQMS-Global, (e) RAQMS-Regional, (f) STEM, and (g) UMD CTM. The dark areas denote regions where the surface pressure is below 850 hPa.

greater CO values than the other models. These results suggest that model output, especially where removed from source regions, is highly dependent on the choice of meteorological input data.

[42] Deep convection is the principal transporter of emissions from the low levels into the upper troposphere. Therefore the placement and intensity of convective mass flux can greatly affect model results. Figure 6 compares distributions of convective mass flux at 850 hPa for 7–31 March. RAQMS and STEM did not report 3-D fields of convective mass flux; thus their data are missing from the figures. Each model shows relative maxima over eastern India, Southeast Asia, and the equatorial Pacific, agreeing with lightning data from the Lightning Imaging Sensor (LIS)

(available at <http://thunder.msfc.nasa.gov>) (Figure 7a) and precipitation patterns from Tropical Rainfall Measuring Mission (TRMM) (available at <http://trmm.gsfc.nasa.gov>) Merged Precipitation data (Figure 7b). On the other hand, Meso-NH shows comparatively weak cloud mass flux over Southeast Asia. Greatest differences among the models are found between 30° and 40°N just east of Japan. Although each model shows enhanced cloud mass flux in this region, FRSGC/UCI and Meso-NH produce larger areas of enhancement and much stronger intensities. The TRMM rainfall totals appear to be greater in this region than over India and Southeast Asia, and there is lightning east of Japan. The results suggest that Meso-NH and FRSGC/UCI give the most realistic results between 30° and 40°N when compared

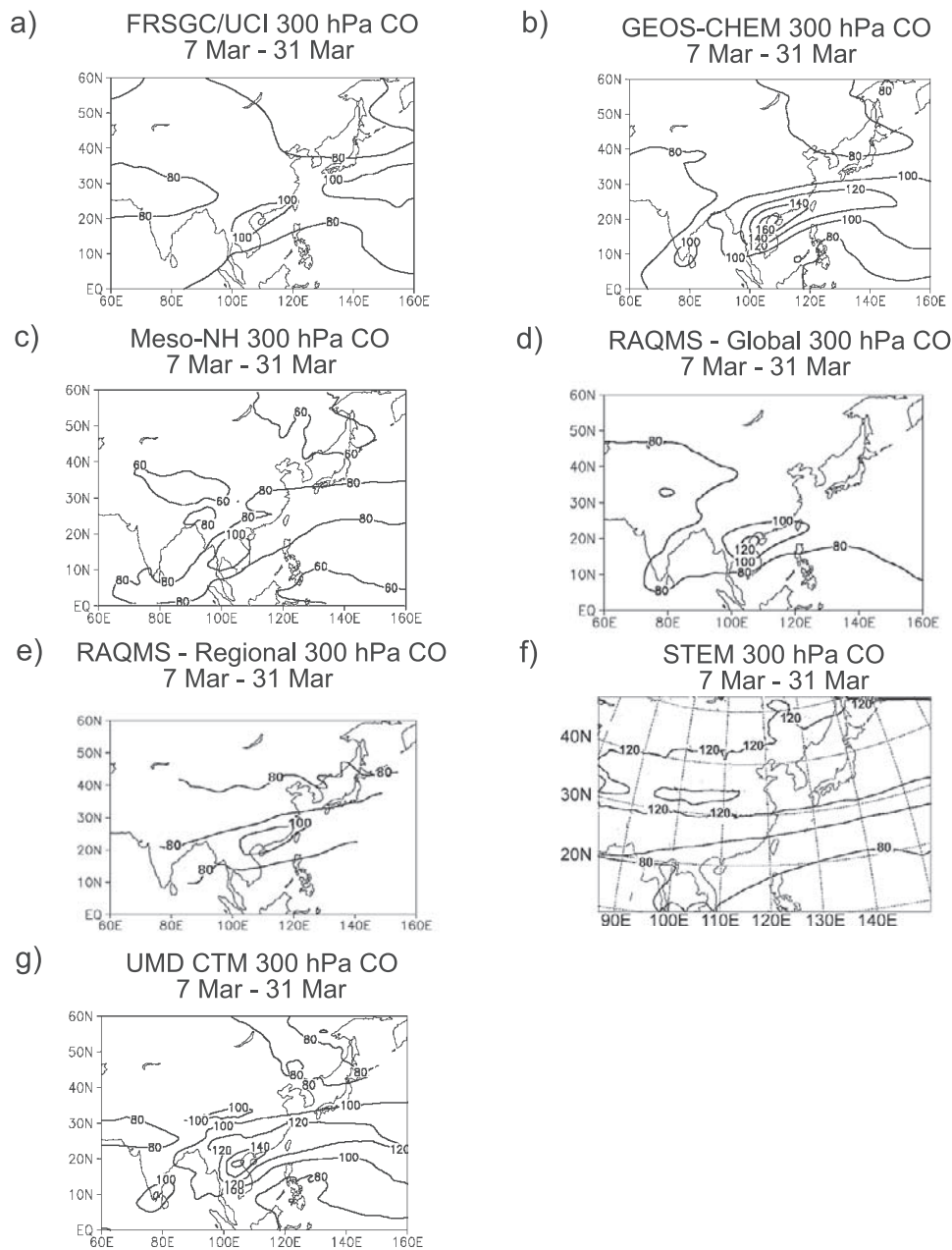


Figure 5. Spatial fields of model-derived CO (ppbv) at 300 hPa for the period 7–31 March. (a) FRSGC/UCI, (b) GEOS-CHEM, (c) Meso-NH, (d) RAQMS-Global, (e) RAQMS-Regional, (f) STEM, and (g) UMD CTM.

with TRMM rainfall and lightning data. The weak fluxes in the GEOS DAS are consistent with its tendency to underestimate convection within midlatitude marine storm tracks [Allen *et al.*, 1997].

[43] In the upper levels, e.g., at 500 hPa (Figure 8), the models show similar patterns of convective mass flux over the equatorial Pacific, central Asia (30°–40°N), and eastern India. However, compared with the other models, FRSGC/UCI produces weaker mass flux over eastern India and much stronger values over Central Asia. It should be noted, however, that the FRSGC/UCI convective mass flux includes, in addition to convection, dry deposition and low-level turbulence. These near-surface effects, rather

than deep convection, seem to cause the much stronger values over Central Asia. In addition, GEOS-CHEM and UMD CTM continue to produce enhanced cloud mass flux over Southeast Asia, a feature not seen at these levels in the other models. We will examine these models' convective mass flux in relation to CO error in section 4.4.

4.2. Pathways of Model CO Error

[44] One of our objectives is to investigate the mechanisms by which the different CTMs, with their individual meteorological input data, simulate the outflow of CO from East Asia during TRACE-P. We specified thresholds to identify locations of significant differences between mod-

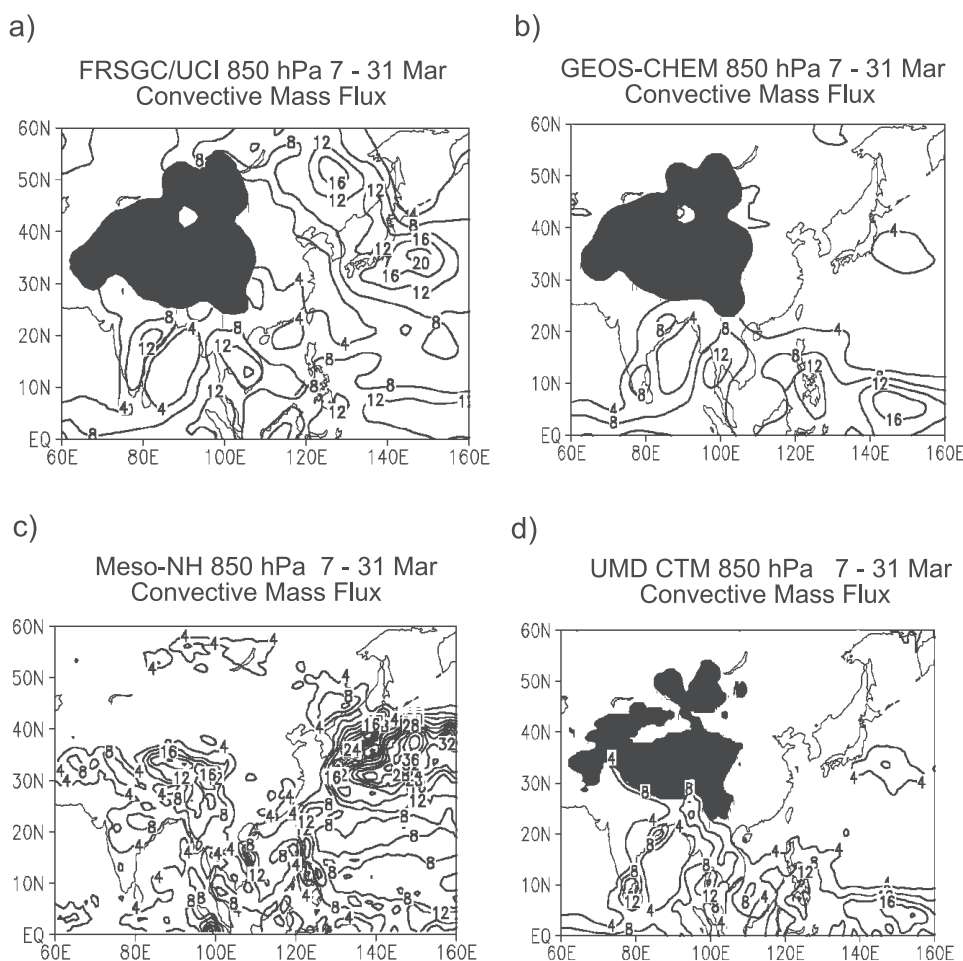


Figure 6. Spatial fields of model-derived convective mass flux ($\times 10^{-3}$ kg/m²/s) at 850 hPa for the period 7–31 March. (a) FRSGC/UCI, (b) GEOS-CHEM, (c) Meso-NH, and (d) UMD CTM. The dark areas denote regions where the surface pressure is below 850 hPa.

eled and aircraft-derived CO and in a later section will investigate possible causes for these differences. Our thresholds were that modeled CO must be (1) 50 ppbv greater than or (2) 100 ppbv less than the measured values. The larger negative threshold is a result of the overall negative bias in model versus aircraft-derived CO.

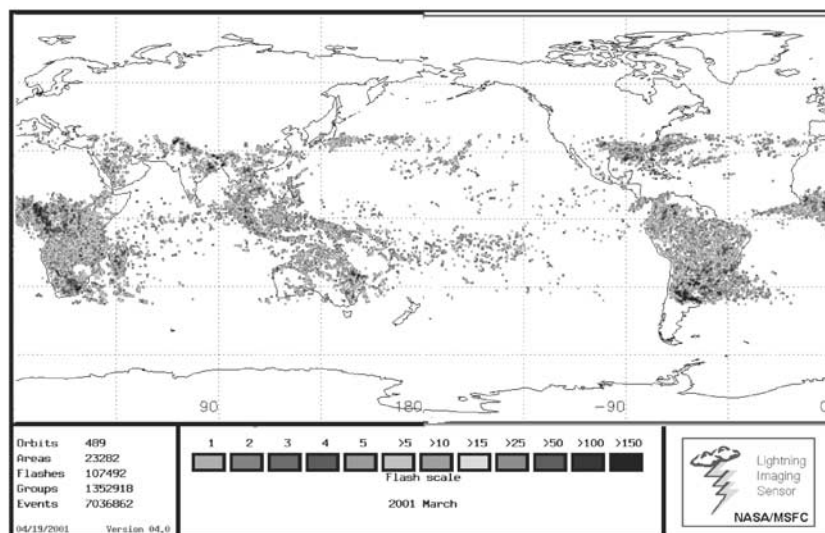
[45] CO error varies somewhat among the models, but trajectories based on FRSGC/UCI CO data are typical of the seven models. Composite 5-day backward trajectories for DC-8 flights 7–17, based on FRSGC/UCI CO error, are shown in Figure 9. Figure 9a shows trajectories from flight track arrival points where modeled CO exceeds the measured value by ≥ 50 ppbv, whereas Figure 9b shows trajectories where modeled CO is less than the measured by at least 100 ppbv. Compared with measured CO, the FRSGC/UCI values are smaller by 100 ppbv (9.6% of total points) more often than they are larger by 50 ppbv (3.6% of total points). Nonetheless, these errors greater than +50 ppbv or smaller than -100 ppbv only represent a small fraction of all the points that were sampled (13.2%). The top panel shows a horizontal perspective, while the lower panel provides pressure altitude versus longitude. The color scheme indicates trajectory altitude, where warmer colors

denote trajectories at relatively high altitudes. Small arrows along the trajectory paths indicate locations at one-day intervals. An “x” at the end of a trajectory indicates that the parcel has exited the data domain before completing the 5-day period. Conversely an asterisk “*” indicates that the trajectory has completed the 5-day period inside the data domain.

[46] Trajectories of model CO errors greater than +50 ppbv (Figure 9a) mostly show air that has traveled over Africa, India, and southern Asia before arriving at flight tracks south of 35°N latitude in the mid levels (<700 hPa, $>10,000$ feet). A smaller number of trajectories originate over the South China Sea at lower levels, first traveling westerly before turning easterly where they reach the flight track. Deep convection is near both sets of trajectories over India and Southeast Asia. Section 4.4 examines how individual models handle this convection, to determine if this is a cause of discrepancy between models and aircraft-derived CO.

[47] For locations where the FRSGC/UCI model-derived CO is at least 100 ppbv too small (Figure 9b), trajectories exhibit two major pathways: those arriving from the northwest and those arriving from the west. In addition, a relatively small number of trajectories arrive from the central

a)



b)

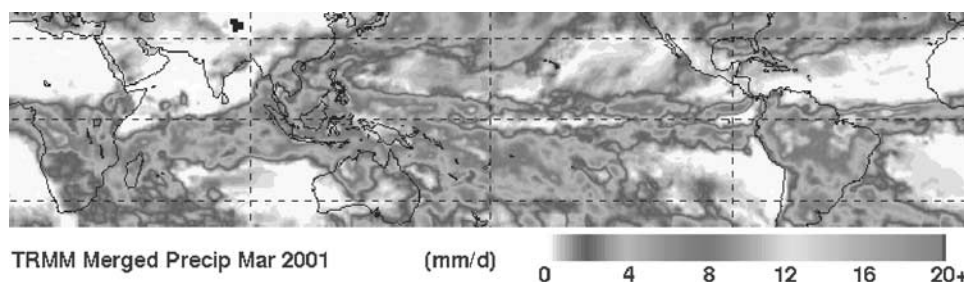


Figure 7. (a) Lightning data for March 2001 from the Lightning Imaging Sensor (LIS) (b) Precipitation data for March 2001 from the Tropical Rainfall Measuring Mission (TRMM). See color version of this figure at back of this issue.

Pacific, and many also originate over the South China Sea, paths seen less often in the +50 ppbv CO error threshold. Parcels arriving from the west exhibit a similar pathway to the -100 ppbv threshold, traveling over Africa, India, and southern Asia; however, they arrive in the upper levels (~300 hPa, ~30,000 feet). Significant convection is not seen near trajectories arriving from the northwest, but the air does travel over heavily industrialized regions (e.g., Shanghai).

4.3. Plume Displacement

[48] Discrepancies in location between simulated and measured plumes are a limitation of current CTMs (Table 3b). Figure 10 shows horizontal distributions of CO at 250 hPa. At 0000 UTC on 27 March (Figure 10a), an area of enhanced CO is seen over eastern China; it moves over southern Japan by 0600 UTC (Figure 10b). The plume is relatively small in size and contains large horizontal gradients. Peak values of this feature are at ~0400 UTC, just as DC-8 flight 15 passes through it, near 125°E. Thus the model produces the plume of enhanced CO; however, there is a small shift in its simulated location compared with its observed location. Therefore the aircraft measures a

value of 229 ppbv whereas FRSGC/UCI provides 111 ppbv, even though the model's nearby peak value is ~160 ppbv. These small shifts in plume location are observed in each of the CTMs throughout the TRACE-P simulations. A survey of other plume events (not shown) indicates that fine horizontal resolution models often simulate the plumes closer to their measured locations than models with coarser horizontal resolution.

4.4. Convective Outflow

[49] Insoluble gases such as CO are transported vertically within convection with negligible loss [Allen *et al.*, 1996b], and with a relatively long lifetime they can travel long distances from the convection. A major objective of DC-8 flight 15 (Figure 10) was to sample middle and high level outflow from intense distant convection over Southeast Asia and China. The DC-8 took off from Yokota (36°N, 139°E), flew southwest to 23°N, 133°E, then headed west to 25°N, 125°E, and finally north over the Yellow Sea (37°N, 125°E). The Yellow Sea leg was designed to sample convective outflow at all levels south of 30°N. The DC-8 then backtracked to 33°N, 125°E,

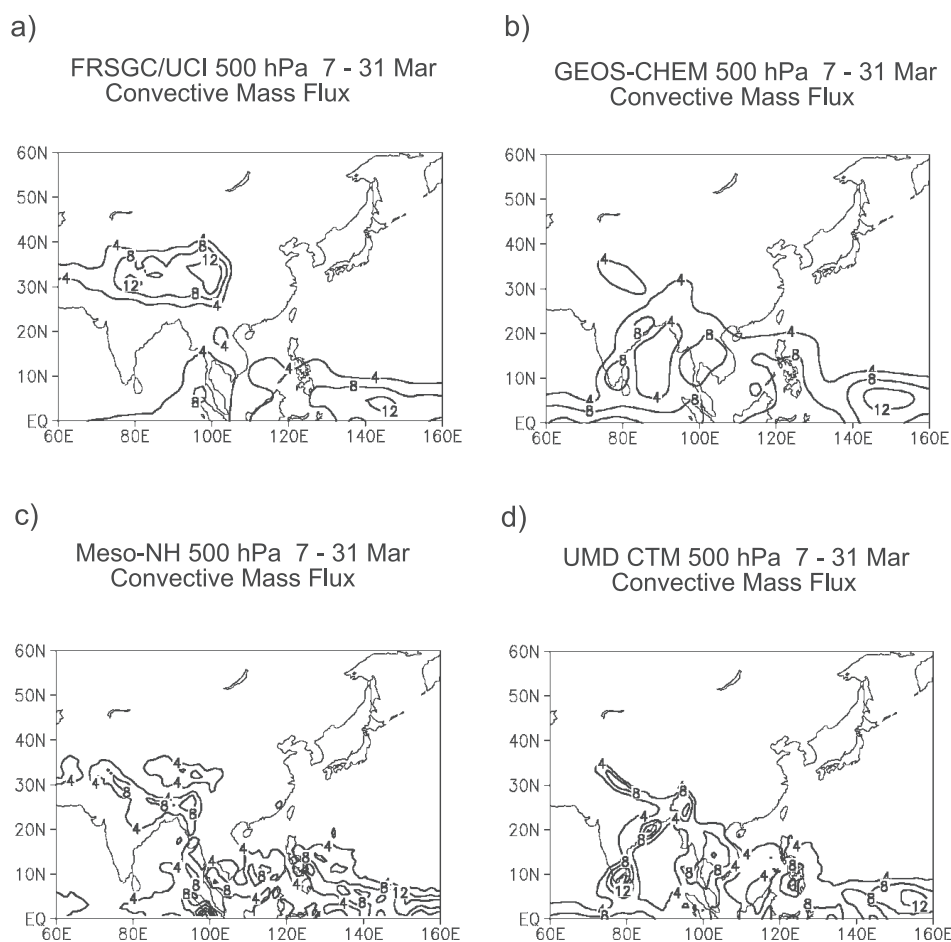


Figure 8. Spatial fields of model-derived convective mass flux ($\times 10^{-3}$ kg/m²/s) at 500 hPa for the period 7–31 March. (a) FRSGC/UCI, (b) GEOS-CHEM, (c) Meso-NH, and (d) UMD CTM.

returning to Yokota around Korea and through the Sea of Japan. Figure 11 shows FSU 5-day backward trajectories for all points along the flight track.

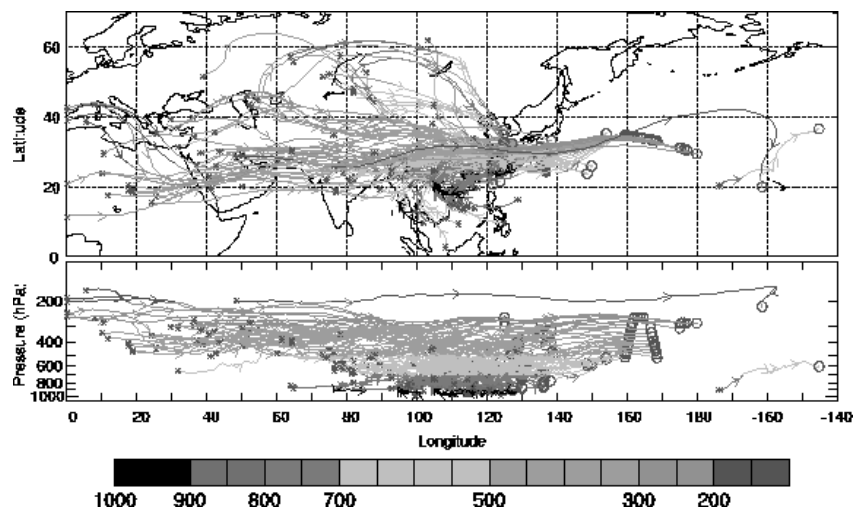
[50] Figure 12 shows Geostationary Meteorological Satellite (GMS) 5 infrared imagery at the time of the flight (0631 UTC 27 March) (Figure 12a) and two days earlier (0631 UTC 25 March) when the trajectories (Figure 11) are near areas of deep convection over Southeast Asia. At flight time (Figure 12a), relatively weak convection is located south of Japan in the region of the flight path, while 2 days earlier (Figure 12b), strong storms are over Southeast Asia and along the east coast of China.

[51] Using the same technique as in the previous section, i.e., trajectory thresholds based on model versus observed CO error, we next investigate the effects of these convective regions on model results. Figure 13 shows 5-day backward trajectories for DC-8 flight 15, based on CO errors from GEOS-CHEM. Trajectories arriving at points along the flight track where modeled CO exceeds the measured value by ≥ 50 ppbv (Figure 13a) originate from the west. Conversely, trajectories arriving at points where modeled CO is less than the measured value by ≥ 100 ppbv (Figure 13b) originate from the northwest. These results are similar to those of the composite 5-day backward trajectories for Flights 7–17 combined, based on FRSGC/UCI CO error (Figure 9).

[52] GEOS-CHEM (Figure 13b) and the other six models (not shown) produce CO errors of ~ -100 ppbv in locations where trajectories arrive from the northwest. These trajectories do not encounter regions of significant convection along their paths (Figure 12), but the air does travel over highly industrialized regions (e.g., Shanghai). The similar CO errors among the models suggest that insufficient emissions may be a cause for the discrepancies between measured and modeled CO. In addition, the models' difficulties in simulating the plumes that are often downwind of these industrialized areas, also may be a factor in causing the differences.

[53] Trajectories arriving from the west (Figure 13a) are quite different. The simulated versus measured CO errors for GEOS-CHEM are larger than those of the other six models. To examine this difference, meteorological data from FRSGC/UCI and GEOS-CHEM are investigated in the convective regions. FRSGC/UCI was chosen because its simulated CO was within ± 10 ppbv of measured values at all trajectory points, whereas GEOS-CHEM exceeded measured values by ≥ 50 ppbv. Convective mass flux from FRSGC/UCI and GEOS-CHEM was interpolated to those trajectory paths where the GEOS-CHEM CO error exceeds measured CO by ≥ 50 ppbv (Figure 13a). Convective mass flux at 6 hourly intervals for six representative trajectories is shown in Figure 14. The color of the lines indicates the

a)

TRACE-P 5 Day Backward Trajectories
FRSGC/UCI CO Error > 50 ppbv

b)

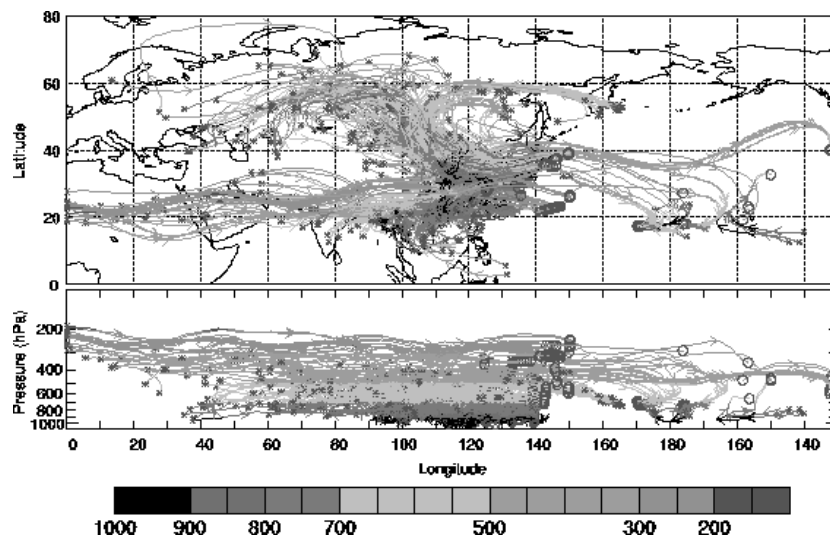
TRACE-P 5 Day Backward Trajectories
FRSGC/UCI CO Error < - 100 ppbv

Figure 9. Five-day backward trajectories for the combination of DC-8 flights 7–17 based on FRSGC/UCI model CO error. (a) FRSGC/UCI model CO is greater than aircraft-derived CO by 50 ppbv or more, (b) FRSGC/UCI model CO is less than aircraft-derived CO by 100 ppbv or more. See color version of this figure at back of this issue.

specific trajectory. Thus each color is used in two lines indicating the same starting point along the flight track (one line for GEOS-CHEM and the other for FRSGC/UCI). Dashed lines represent results from FRSGC/UCI, while solid lines show plots from GEOS-CHEM. The limitations of this methodology must be acknowledged. Convection reduces air mass integrity since updrafts and downdrafts within the convective column will mix air masses of different histories. Thus one can be confident in a trajectory reaching an initial convective area but less certain about

any prior paths or convective encounters. Nonetheless, we believe this approach provides informative results.

[54] Figure 14 reveals large differences in convective mass flux between FRSGC/UCI and GEOS-CHEM. One should recall that the FRSGC/UCI (GEOS-CHEM) convective mass fluxes are from the ECMWF (GEOS DAS). From flight time until ~ 36 hours back, most trajectories travel over water (Figure 13a) where there are no emissions. However, the trajectories indicate air traveling near convective regions of Southeast Asia at ~ 42 hours back in time

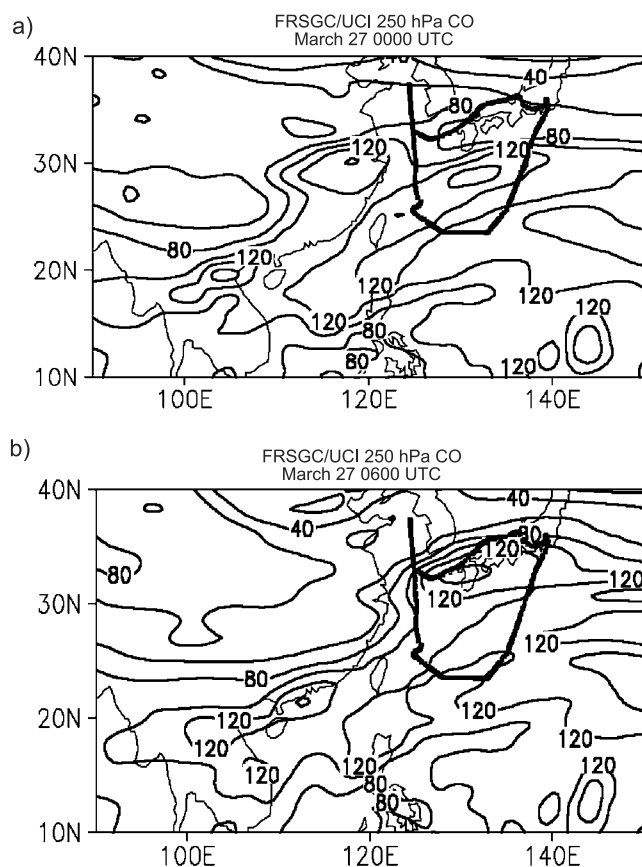


Figure 10. Spatial fields of FRSGC/UCI model-derived CO (ppbv) at 250 hPa for (a) 27 March at 0000 UTC and (b) 27 March 0600 UTC. DC-8 flight 15 track is superimposed on the figure.

and over eastern India at ~ 60 hours previous. Large differences in convective mass flux are seen during both encounters. These differences are important because there was significant biomass burning in these regions (Figure 1). The stronger convective mass flux of GEOS-CHEM (solid lines) provides more meteorological lift for these emissions to enter the free troposphere. This enhanced lift over Southeast Asia and eastern India may be the reason why the GEOS-CHEM-derived CO exceeds measured values by ≥ 50 ppbv at these points along flight 15. Conversely, FRSGC/UCI, with weaker convective mass flux, simulates CO within ± 10 ppbv of aircraft-derived values.

[55] Distributions of convective mass flux at 850 and 500 hPa on 25 March at 0600 UTC for GEOS-CHEM and FRSGC/UCI (Figure 15) show that the results described in Figure 14 are representative for this particular flight. Convective mass flux from GEOS-CHEM is much stronger than from FRSGC/UCI at all levels over Southeast Asia and eastern India. However, GEOS-CHEM does not exhibit a systematic bias in overestimating convective mass flux for all DC-8 flights. Referring back to convective mass flux for the period 7–31 March (Figures 6 and 8), GEOS-CHEM's results generally are similar to the other models. Therefore it is thought that DC-8 flight 8 is a particular case when GEOS-CHEM overestimates the convection, and is not a consistent problem with the model. This result is in contrast with *Allen*

et al. [1997], who showed that an earlier version of GEOS DAS (GEOS-1) overestimated the frequency and extent of convection in subtropical regions such as Southeast Asia. As stated previously, a major objective of this flight was to sample intense distant convection. The intensity of this convection is thought to be a cause of GEOS-CHEM's overestimation. These results emphasize the importance of convective mass flux in chemical transport models.

4.5. Boundary Layer Depth

[56] Boundary layer depth plays an important role in either capping or ventilating surface based pollutants. A major objective of DC-8 Flight 13 (Figure 16) was to sample dust and pollution outflow near the China coast. The DC-8 departed Yokota, Japan, flew southwest and crossed a weak front, then northwest recrossing the front, and finally north over the Yellow Sea before returning to Yokota. The leg over the Yellow Sea was within the boundary layer. Considerable Asian pollution was encountered along this leg, including a well-defined crossing of the Shanghai plume near 29°N where measured CO reached 1240 ppbv (Figure 3c).

[57] Figure 17 is a time series focusing on the Shanghai plume, including aircraft altitude, measured CO, and the seven model-derived values. It is a close-up of a portion of Figure 3c. Although each model locates the intense Shanghai plume within $\sim 1^\circ$ latitude, they greatly underestimate its intensity. Vertical cross sections of CO along the northern leg of flight 13 are shown in Figure 18. Results from the STEM mesoscale CTM (Figure 9a) and the GEOS-CHEM global CTM (Figure 18b) illustrate these models' simulation of this intense event. Both CTMs produce areas of enhanced CO near the surface from 25°N to 34°N . However, the intensity and exact placement of these areas vary. Horizontal distributions of CO at flight time, 0600 UTC 21 March (Figure 19), reveal that the enhanced region consists of two distinct plumes. The northern maximum ($\sim 30^\circ\text{N}$) represents the Shanghai plume, while the southern portion ($\sim 26^\circ\text{N}$) represents outflow from southern China. Although both plumes are located in eastern China, their vertical structures are quite different (Figures 18–19). The Shanghai plume is shallower (~ 950 hPa versus ~ 700 hPa) and has slightly greater CO than the southern plume.

[58] We investigated flow patterns and vertical thermal stratification to determine possible causes for the plumes' differing altitudes. The relatively weak front in Figure 16 is orientated northeast to southwest off the China coast. At the site of the Shanghai plume, there is a weak stable layer associated with the front at 850 hPa (not shown). This height corresponds closely to the top of the aircraft-documented haze layer near the Shanghai plume (~ 800 hPa, ~ 7000 feet). A large anticyclone over Asia produces the offshore flow that dominates eastern China during most of the cold season [*Fuelberg et al.*, 2003]. And, the postfrontal winds act to reinforce this eastward flow.

[59] The models' boundary layer depth was examined near the plumes, with PBL heights from GEOS-CHEM shown in Figure 20. The PBL height ranges from 950 to 925 hPa over eastern China and the Yellow Sea. Thus the PBL appears to cap the Shanghai plume. That is, surface emissions are prevented from being transported higher into the free troposphere. On the other hand, the southern plume,

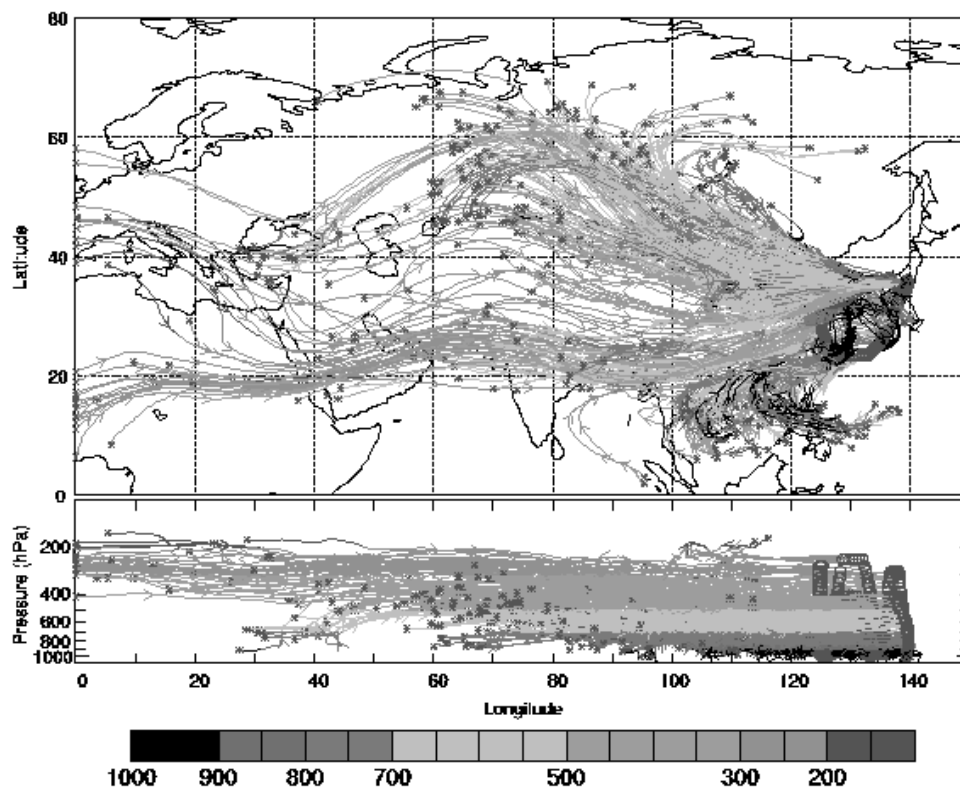
TRACE-P 5 Day Backward Trajectories
DC-8 Flight 15

Figure 11. Five-day backward trajectories for DC-8 flight 15. See color version of this figure at back of this issue.

extending to ~ 700 hPa (Figures 18–19), extends considerably higher than the shallow PBL.

[60] Horizontal distributions of CO two days prior to flight time (0600 UTC 19 March, Figure 21) show origins of the two plumes. The Shanghai plume is a localized feature that originates near this coastal city. However, the southern plume does not appear to be localized. Instead, horizontal advection of CO occurs at all levels up to 700 hPa. Thus this area of enhanced CO seems to have been transported vertically near its source at some earlier time and therefore was not affected by the locally low PBL near the China coast. Conversely, PBL depth is very important to the Shanghai plume because it is produced by local emissions. The models do a good job of simulating the shallow PBL near Shanghai. Therefore the underestimation and spatial smoothing of local Shanghai emissions within the models appear to be the cause of the discrepancy between model-derived and simulated results.

5. Summary and Conclusions

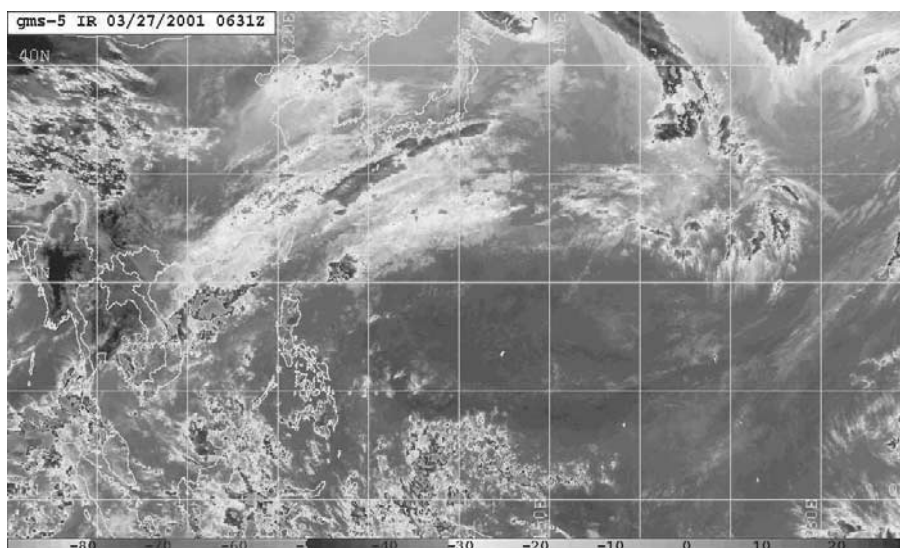
[61] NASA's Transport and Chemical Evolution over the Pacific (TRACE-P) experiment, conducted between February and April 2001, sought to characterize the chemical composition of Asian outflow and describe its evolution over the Pacific Basin. In addition to in situ chemical measurements by two NASA aircraft (a DC-8 and P-3B), TRACE-P included a major support activity from several

3-D chemical transport models (CTMs) that were used in real time to optimize flight strategies. This paper has described an intercomparison and evaluation of CO from seven 3-D CTMs that were run during TRACE-P. Each of the six modeling groups provided special post-mission simulations for the intercomparison, using the same common set of emissions data.

[62] We first statistically analyzed the aircraft-derived and seven numerically derived versions of CO. Values of model simulated CO were interpolated to the locations, altitudes, and times along each of the DC-8 flight tracks where measurements were made. The collocated measured and simulated values were used to calculate mean differences, RMS differences, correlations and slopes.

[63] The results for combined DC-8 flights 7–17 showed that values of model simulated CO generally were similar to measured values for the smaller values of CO, but they tended to diverge at greater values. The models showed an overall negative bias, with mean differences from measured values ranging from -67.3 to 14.6 ppbv. This negative bias may reflect an underestimate of the prescribed CO emissions sources. Correlations for the four global models ranged from 0.56 to 0.75, while correlations for the three regional models ranged from 0.44 to 0.61. Statistics from the global models did not differ greatly from those of the regional models, suggesting that increased model resolution does not necessarily produce better statistics with respect to measurements. However,

a)



b)

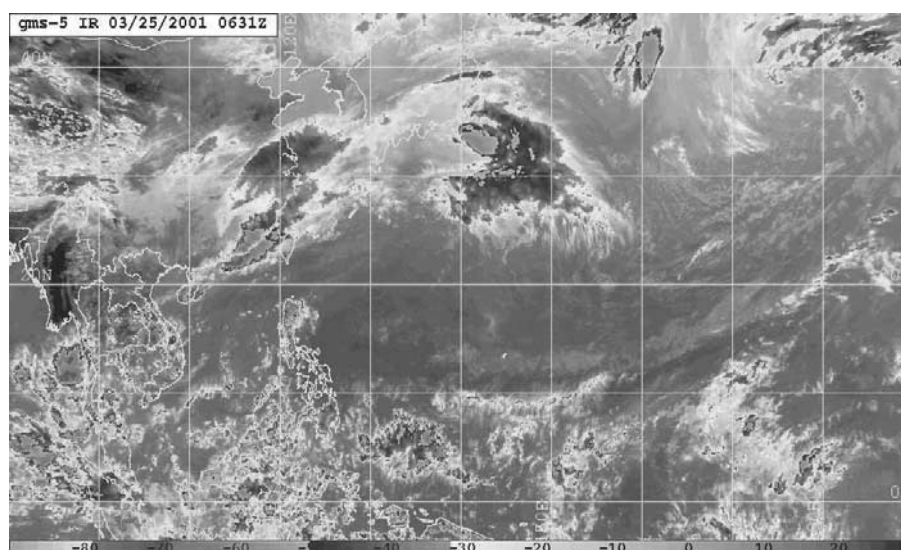


Figure 12. Infrared imagery from Geostationary Meteorological Satellite (GMS) 5 (a) at the time of flight 15 (0631 UTC 27 March) and (b) two days prior to flight 15 (0631 UTC 25 March). See color version of this figure at back of this issue.

statistics for secondary plume pollutants such as photochemically produced ozone may show a different behavior with different model resolutions since averaging of fine-scale features in global models which are present in regional models, may lead to different net ozone production rates over a region.

[64] The statistical agreements varied greatly among the individual flights. However, for each given flight, the models generally provided similar relative statistical results. Three flights were described in detail. DC-8 flight 8 was illustrated because its seven simulations were consistently among the best. Models produced RMS differences of ~ 40 ppbv and correlations near 0.80. This flight exhibited

few spikes or plumes of CO. The models were most consistent in areas of relatively small CO. DC-8 flight 10 exhibited some of the greatest discrepancies among the models. Most models performed poorly, with correlations ranging from 0.13 to 0.71. Overestimating the amplitude of a midtropospheric CO peak, while greatly underestimating the amplitude of a boundary layer peak, was shown to be a limitation of some models. The model that produced the best correlation had fairly constant CO throughout the flight, which averaged out to the best result. The greatest measured CO occurred during flight 13 over the Yellow Sea. The various models generally did a good job of simulating CO for this flight. Each model correctly located

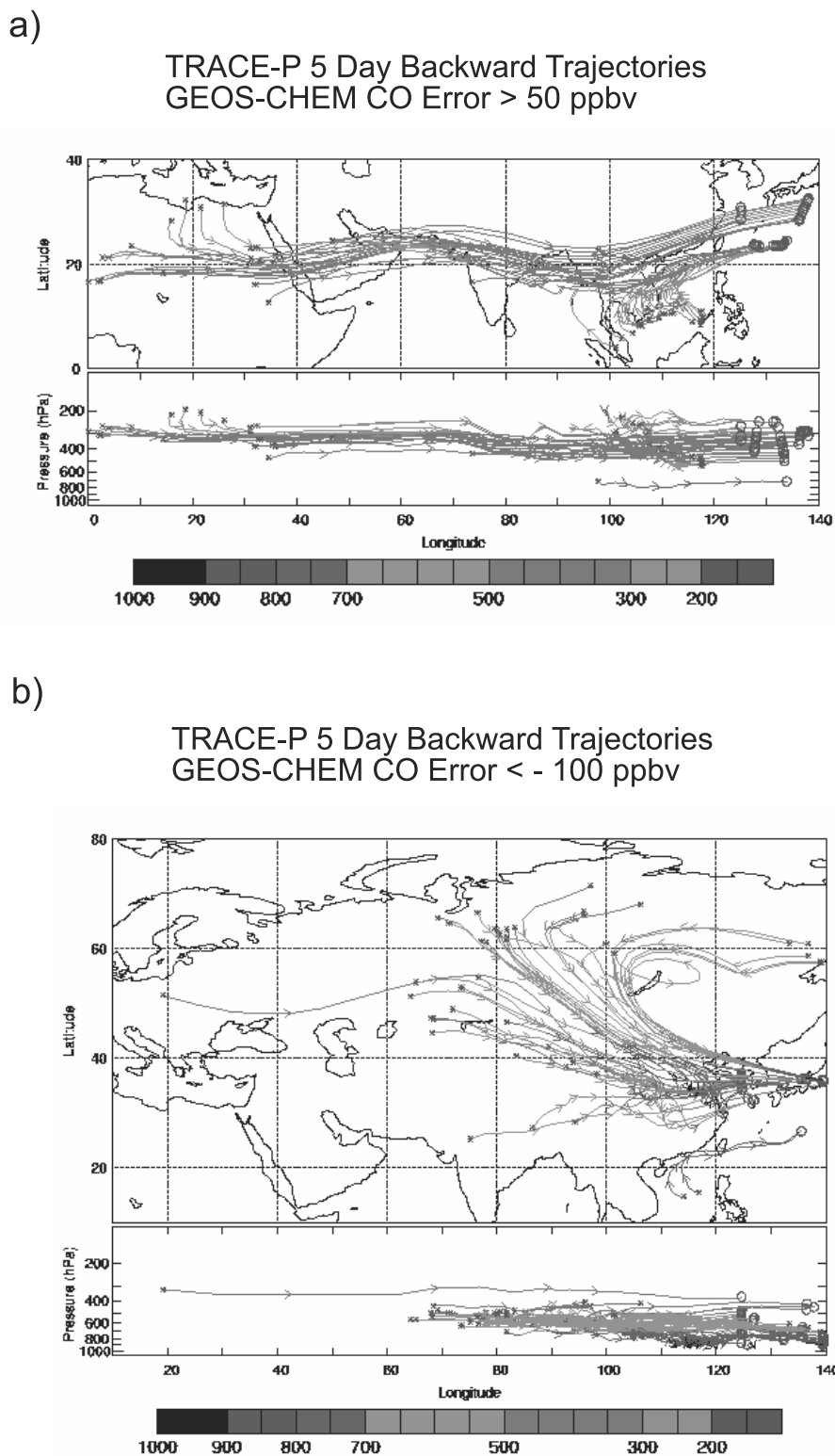


Figure 13. Five-day backward trajectories for DC-8 flight 15 based on GEOS-CHEM model CO error. (a) GEOS-CHEM model CO is greater than aircraft-derived CO by 50 ppbv or more, (b) GEOS-CHEM model CO is less than aircraft-derived CO by 100 ppbv or more. See color version of this figure at back of this issue.

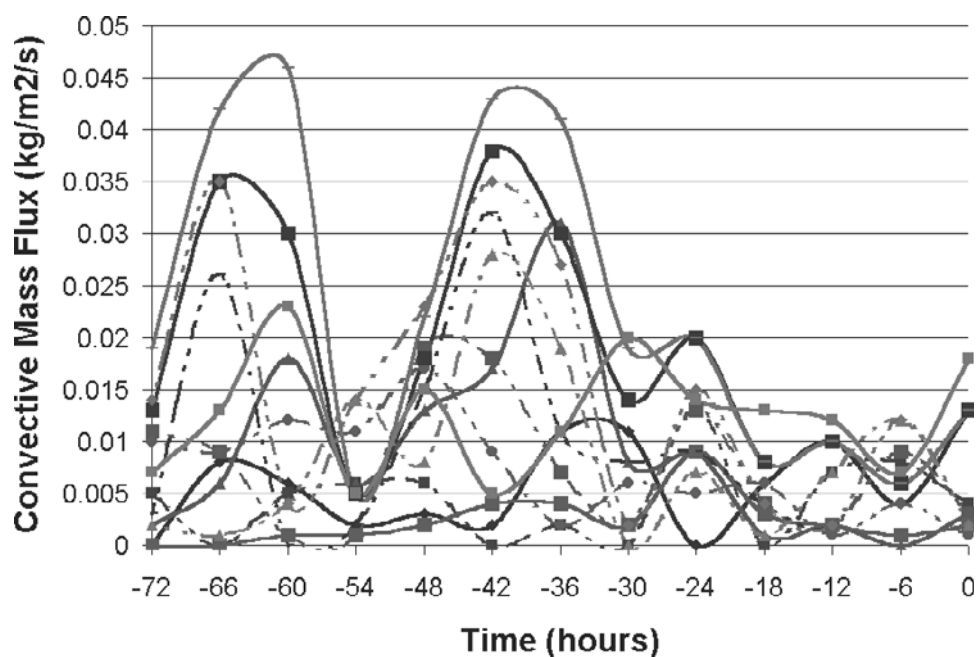


Figure 14. Convective mass flux at 6 hourly intervals for six representative trajectories based on GEOS-CHEM CO exceeding the measured value by 50 ppbv or more during DC-8 flight 15. Results are shown for GEOS-CHEM (solid line) and FRSGC/UCI (dashed line). The color of each line indicates the specific trajectory. Thus each color is used in two lines indicating the same starting point along the flight track (one for GEOS-CHEM and one for FRSGC/UCI). See color version of this figure at back of this issue.

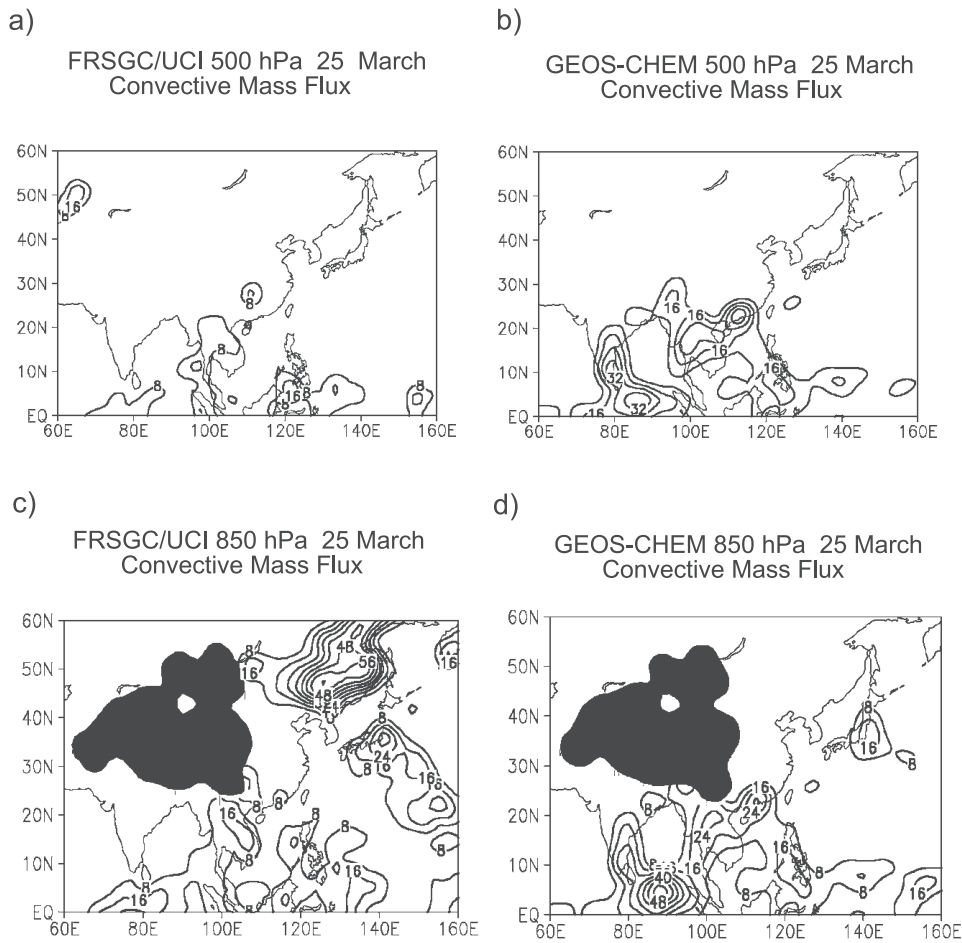


Figure 15. Spatial fields of model-derived convective mass flux ($\times 10^{-3} \text{ kg/m}^2/\text{s}$) for 0600 UTC 25 March; at 500 hPa (a) FRSGC/UCI, (b) GEOS-CHEM and at 850 hPa (c) FRSGC/UCI, and (d) GEOS-CHEM. The dark areas denote regions where the surface pressure is below 850 hPa.

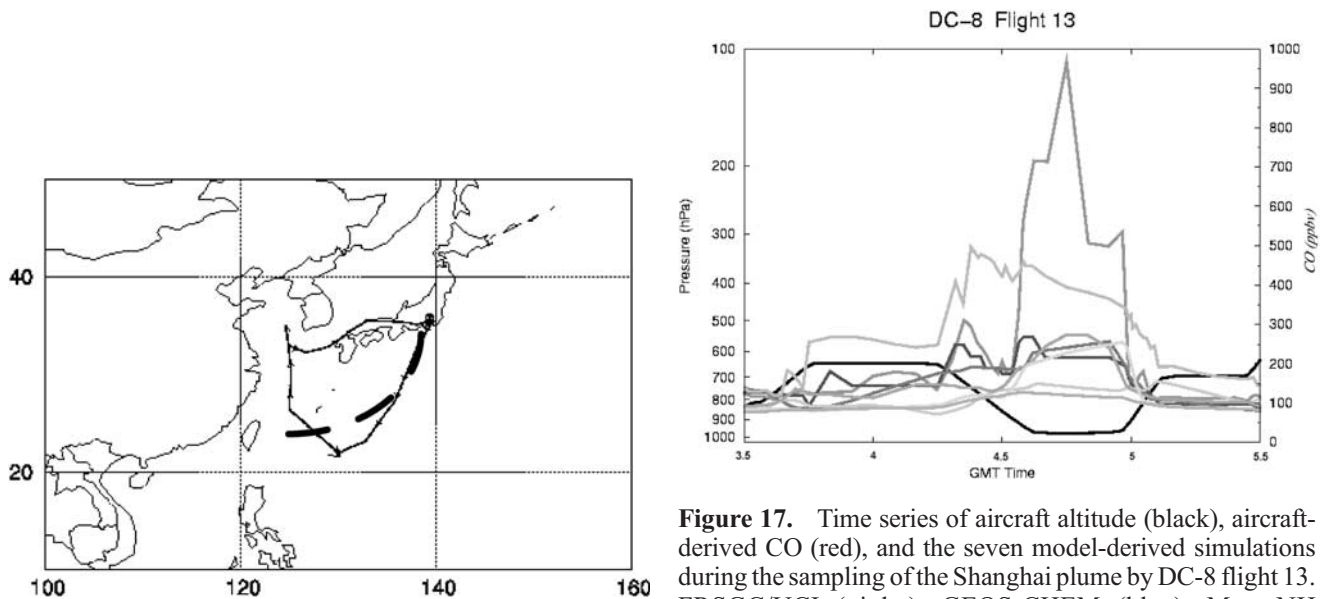


Figure 16. Flight track of DC-8 flight 13 (Yokota Local 1). The position of the cold front is shown by the long dashed lines.

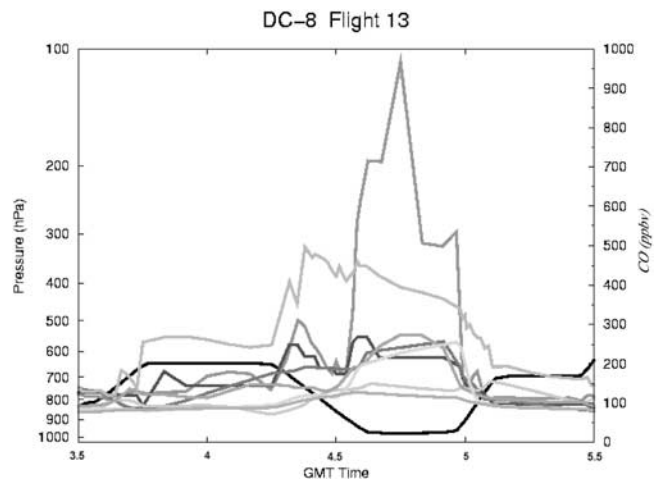


Figure 17. Time series of aircraft altitude (black), aircraft-derived CO (red), and the seven model-derived simulations during the sampling of the Shanghai plume by DC-8 flight 13. FRSGC/UCI (violet), GEOS-CHEM (blue), Meso-NH (green), RAQMS-Global (brown), RAQMS-Regional (cyan), STEM (orange), and UMD CTM (pink). See color version of this figure at back of this issue.

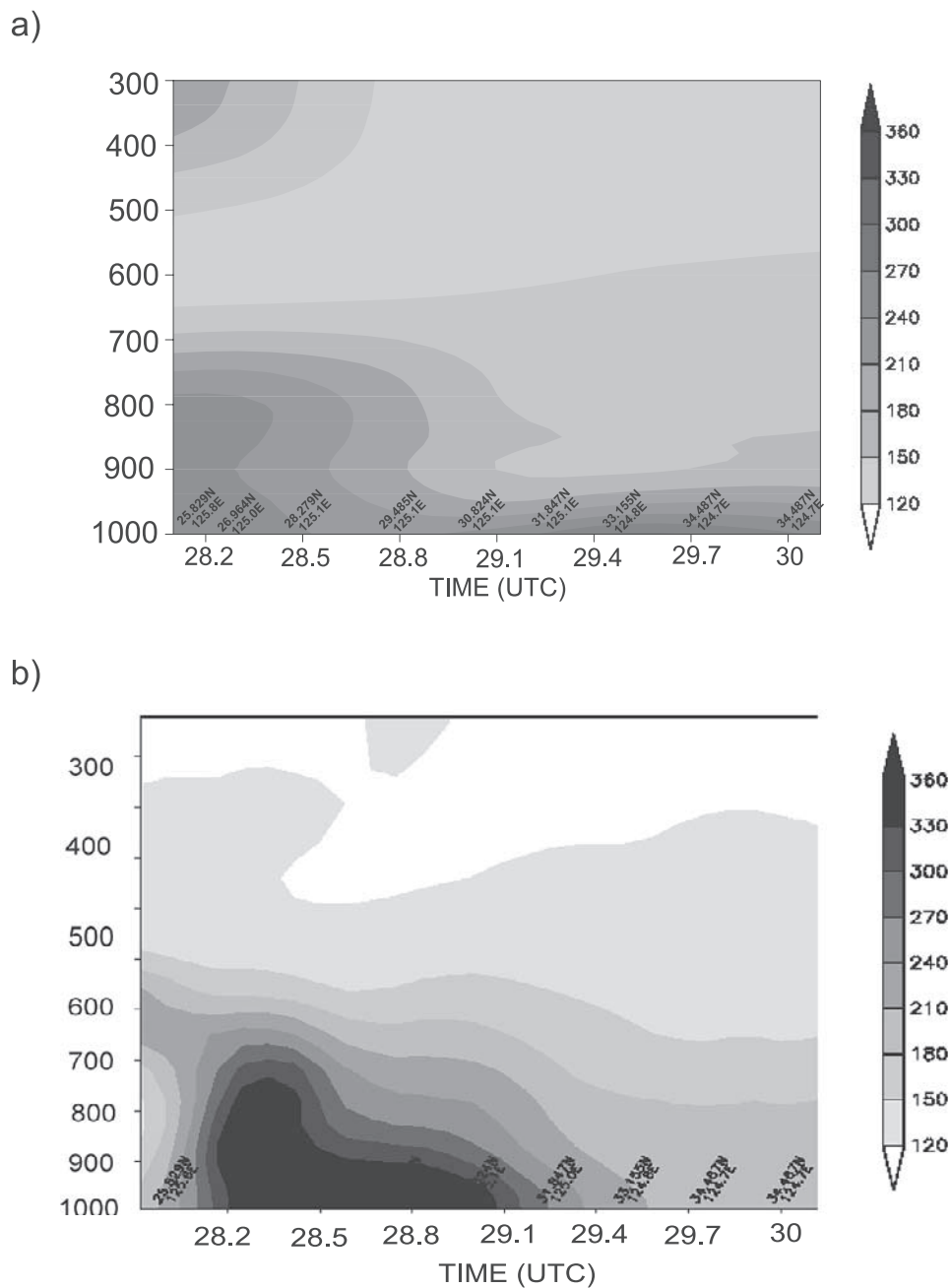


Figure 18. Vertical cross sections of CO along the northern leg of DC-8 flight 13 from (a) GEOS-CHEM and (b) STEM.

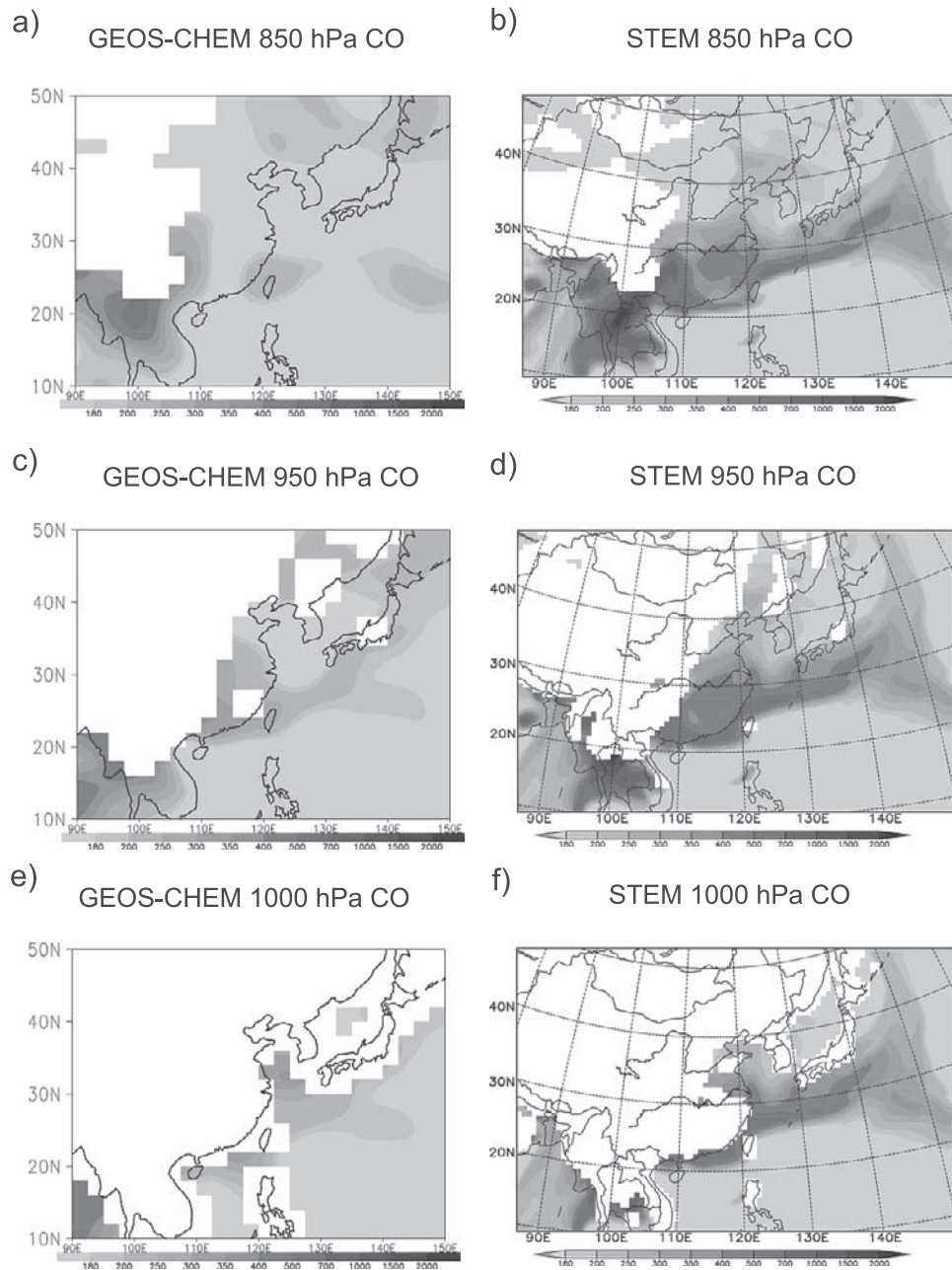


Figure 19. Spatial fields of model-derived CO (ppbv) for 0600 UTC 21 March from GEOS-CHEM at (a) 850 hPa, (c) 950 hPa, (e) 1000 hPa, and from STEM at (b) 850 hPa, (d) 950 hPa, (f) 1000 hPa.

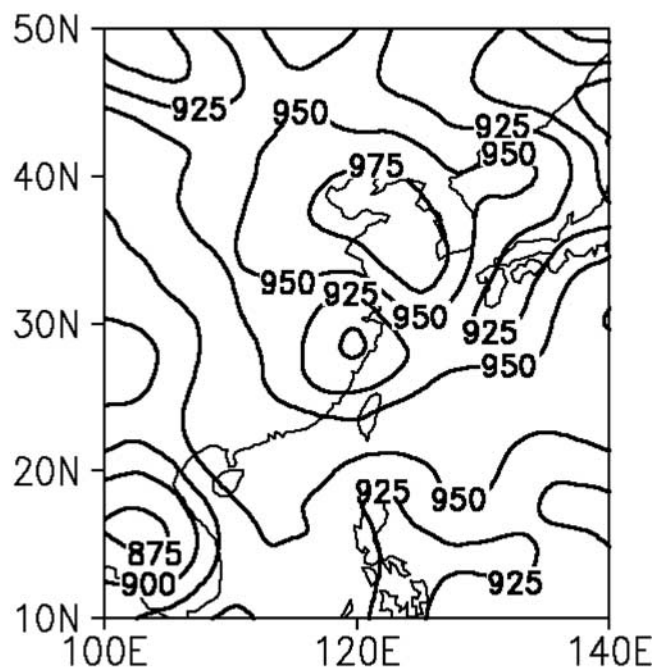


Figure 20. Simulated PBL heights (hPa) from GEOS-CHEM at 0600 UTC 21 March.

the intense Shanghai plume that was sampled on two flight legs, but all models greatly underestimated its intensity.

[65] The models' difficulties in simulating the intense plumes during DC-8 flight 13 prompted further investigation. We defined a plume using the criterion that the sampled air must exhibit CO values that were enhanced at least 20 ppbv above the local background. These results differed noticeably from those based on all measurements. For example, RMS differences generally were greater than 200 ppbv for plumes, versus a range from 41 to 128 ppbv for all segments. Discrepancies between simulated and measured plumes were due both to shifts in their physical placement and their magnitudes.

[66] We investigated whether there was a relationship between CO error and altitude by dividing the atmosphere into five layers. Greatest mean differences and RMS differences against measured values were found in the lower levels. This was expected since many plumes are located at these altitudes. Smaller correlations were found in the upper levels for most models. This indicates that the models may be unable to simulate the meteorological ascent that is needed to pump CO from its source region at the surface to the upper levels at correct times and locations. Also, since CO at higher altitudes is more influenced by sources outside of the immediate TRACE-P region, this may have caused difficulties for the regional CTMs.

[67] We next investigated the mechanisms by which the different CTMs, with their differing meteorological input data, simulated the outflow of CO from East Asia during TRACE-P. Three-dimensional model-derived CO data at 6 hourly intervals were provided for the entire TRACE-P period. Several modeling groups also provided parameters describing boundary layer processes and deep convection which could be compared with satellite imagery, rainfall totals, and lightning data.

[68] Horizontal distributions of CO averaged over the TRACE-P period provided a useful intercomparison of model results. The models best agreed on the placement and intensity of CO at low levels, i.e., close to the surface-based emission sources. In the upper levels, e.g., 300 hPa, all models showed similar distributions; however, the overall intensity of their CO varied widely. The two CTMs that used closely related meteorological input data exhibited very similar results. This finding suggests that model output, especially where removed from source regions, is highly dependant on the choice of initial meteorological input data.

[69] Thresholds were specified to identify locations of significant differences between modeled and measured CO. Five-day backward trajectories based on model CO error were calculated for the combination of flights 7–17. Using results from FRSGC/UCI as a representative example, trajectories from those points along the flight tracks where model CO error exceeded the measured value by ≥ 50 ppbv were found to arrive generally from the west. Conversely, trajectories of model CO errors ≤ -100 ppbv more often arrived from the northwest.

[70] DC-8 flight 15 was investigated to determine possible causes for differences between model and aircraft-derived CO. Using results from GEOS-CHEM as an example, trajectories from this flight showed similar paths as those for the combination of DC-8 flights 7–17. That is, trajectories arriving at points where GEOS-CHEM CO was less than the measured CO by ≤ -100 ppbv originated from the northwest. These parcels had traveled over heavily industrialized areas, including Shanghai. Since each of the seven models produced similar CO errors for these points, insufficient CO emissions may be a cause for the underestimates. Trajectories arriving at points along the flight track where modeled CO exceeded measured CO by ≥ 50 ppbv originated from the west, having traveled over areas of deep convection in Southeast Asia and eastern India. Only one model produced CO exceeding the measured value by ≥ 50 ppbv for these points along the flight track. This model was found to have much stronger convective mass flux than the other models near Southeast Asia and eastern India. Strong biomass burning was located in both areas at the time. Thus the strong convective mass flux in regions of strong emissions may have caused the model to produce CO that exceeded the measured values.

[71] DC-8 flight 13 was investigated to examine meteorological processes affecting the models' simulation of the intense Shanghai plume. The Shanghai plume was found to be a localized feature originating near that city. A large anticyclone over Asia was responsible for offshore flow that dominated the region. The models' simulated PBL ranged from 950 to 925 hPa over eastern China and the Yellow Sea. The PBL was shown to cap the Shanghai plume, confining heavy pollution to the very lowest levels. A nearby secondary area of enhanced CO, reaching 700 hPa, was not affected by the local PBL values. Unlike the Shanghai plume, this enhanced CO was transported aloft at some distant location and therefore was not influenced by the PBL in eastern China.

[72] Although this study did not consider the chemistry of the seven CTMs, those aspects undoubtedly played a role in producing CO differences among the models and compared

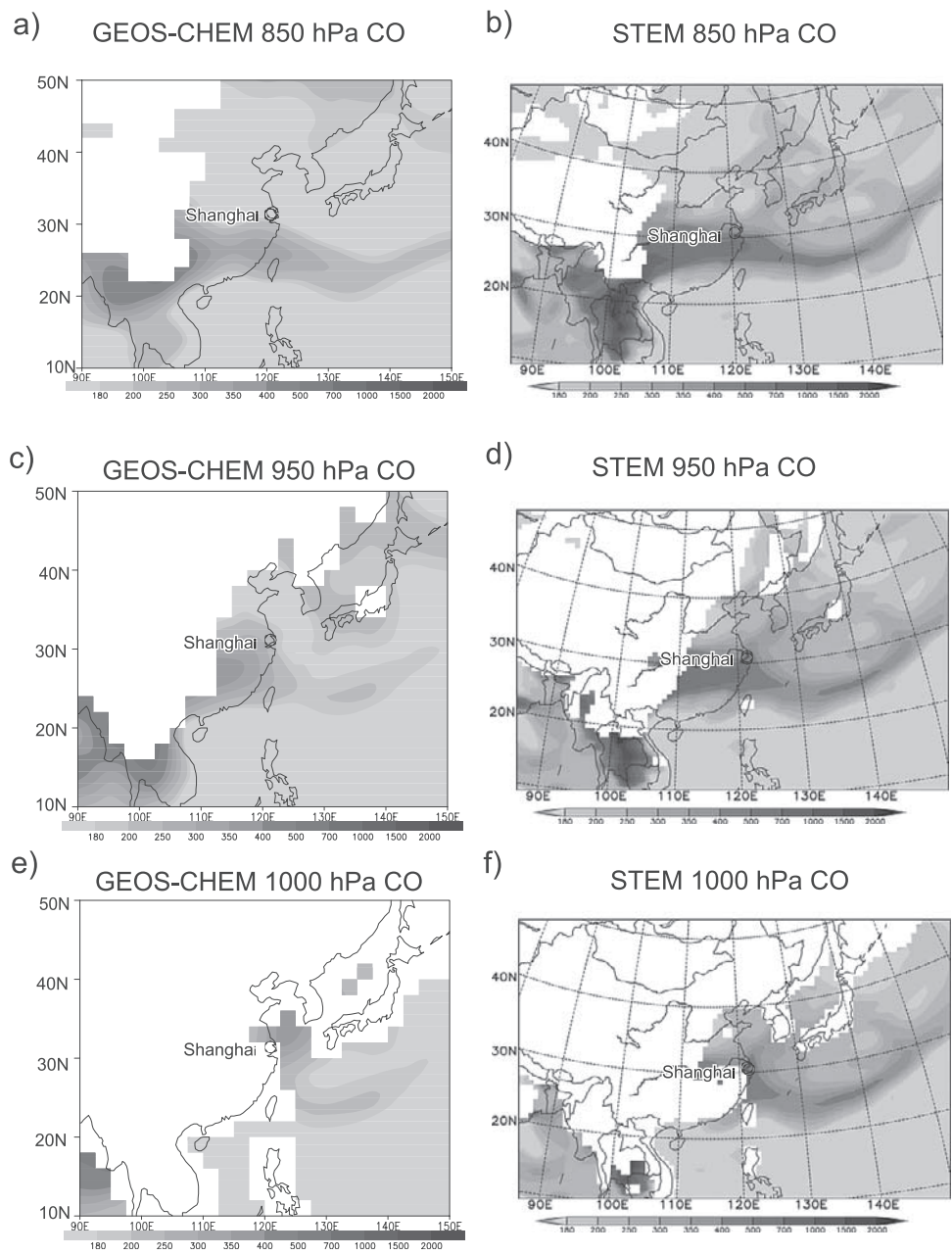


Figure 21. Spatial fields of model-derived CO (ppbv) for 0600 UTC 19 March from GEOS-CHEM at (a) 850 hPa, (c) 950 hPa, (e) 1000 hPa, and from STEM at (b) 850 hPa, (d) 950 hPa, and (f) 1000 hPa. The location of Shanghai is denoted by the shaded diamond.

to observations. Nonetheless, current results document the importance of meteorological processes within chemical transport models. The handling of convection and boundary layer processes especially appear to have a major impact on model results.

[73] **Acknowledgments.** This research was sponsored by the NASA Tropospheric Chemistry Program. We express our sincere appreciation to the support personnel in each of the modeling groups that participated in this study. Although too numerous to mention, these individuals were vital to the research.

References

- Allen, D. J., R. B. Rood, A. M. Thompson, and R. D. Hudson, Three-dimensional radon-222 calculations using assimilated meteorological data and a convective mixing algorithm, *J. Geophys. Res.*, **101**, 6871–6881, 1996a.
- Allen, D. J., P. Kasibhatla, A. M. Thompson, R. B. Rood, B. G. Doddridge, K. E. Pickering, R. D. Hudson, and S.-J. Lin, Transport-induced interannual variability of carbon monoxide determined using a chemistry and transport model, *J. Geophys. Res.*, **101**, 28,655–28,669, 1996b.
- Allen, D. J., K. E. Pickering, and A. Molod, An evaluation of deep convective mixing in the Goddard Chemical Transport Model using International Satellite Cloud Climatology Project cloud parameters, *J. Geophys. Res.*, **102**, 25,467–25,476, 1997.
- Allen, D. J., K. E. Pickering, G. Stenchikov, A. Thompson, and Y. Kondo, A three-dimensional total odd nitrogen (NO_y) simulation during SONEX using a stretched-grid chemical transport model, *J. Geophys. Res.*, **105**, 3851–3876, 2000.
- Al-Saadi, J. A., R. B. Pierce, T. D. Fairlie, M. M. Kleb, R. S. Eckman, W. L. Grose, M. Natarajan, and J. R. Olson, Response of middle atmosphere chemistry and dynamics to volcanically elevated sulfate aerosol: Three-dimensional coupled model simulations, *J. Geophys. Res.*, **106**, 27,255–27,275, 2001.
- Bey, I., et al., Global modeling of tropospheric chemistry with assimilated meteorology: Model description and evaluation, *J. Geophys. Res.*, **106**, 23,073–23,095, 2001.
- Carmichael, G. R., L. K. Peters, and T. Kitada, A second generation model for regional scale transport/chemistry/deposition, *Atmos. Environ.*, **20**, 173–188, 1986.
- Carmichael, G. R., L. K. Peters, and R. D. Saylor, The STEM-II regional scale acid deposition and photochemical oxidant model-I. An overview of model development and applications, *Atmos. Environ.*, **25A**, 2077–2090, 1990.
- Carmichael, G. R., et al., The MICS-Asia study: Model intercomparison of long range transport and sulfur deposition in East Asia, *Atmos. Environ.*, **36**, 175–199, 2002.
- Carmichael, G. R., Y. Tang, G. Kurata, I. Uno, D. G. Streets, J. H. Woo, H. Huang, and J. Yienger, Regional-scale chemical transport modeling in support of intensive field experiments: Overview and analysis of the TRACE-P observations, *J. Geophys. Res.*, **108**(D21), 8823, doi:10.1029/2002JD003117, in press, 2003.
- Carter, W. P. L., Documentation of the SPARC-99 chemical mechanism for VOC reactivity assessment final report to California Air Resources Board, *Tech. Rep.*, Univ. of California, Riverside, Riverside, Calif., 2000.
- Carver, G. D., P. D. Brown, and O. Wild, The ASAD atmospheric chemistry integration package and chemical reaction database, *Comput. Phys. Comm.*, **105**, 197–215, 1997.
- Colella, P., and P. R. Woodward, The piecewise parabolic method (PPM) for gas-dynamical solutions, *J. Comput. Phys.*, **54**, 174–201, 1984.
- De Gouw, J. A., C. Warneke, H. A. Scheeren, C. van der Veen, M. Bolder, M. P. Scheele, J. Williams, S. Wong, L. Lange, H. Fischer, and J. Lelieveld, Overview of the trace gas measurements on board the Citation aircraft during the intensive field phase of INDOEX, *J. Geophys. Res.*, **106**, 28,453–28,468, 2001.
- Duncan, B. N., R. V. Martin, A. C. Staudt, R. Yevich, and J. A. Logan, Interannual and seasonal variability of biomass burning emissions constrained by satellite observations, *J. Geophys. Res.*, **108**(D2), 4100, doi:10.1029/2002JD002378, 2003.
- Environmental Protection Agency, National air pollutant emission trends, 1990–1996, *Tech. Rep.*, Washington, D. C., 1997.
- Fox-Rabinovitz, M. S., L. L. Takacs, and R. C. Govindaraju, A variable resolution stretched grid general circulation model and data assimilation system with multiple areas of interest: Studying anomalous regional climate events of 1998, *J. Geophys. Res.*, **107**(D24), 4768, doi:10.1029/2002JD002177, 2002.
- Fuelberg, H. E., C. M. Kiley, J. R. Hannan, D. J. Westberg, M. A. Avery, and R. E. Newell, Meteorological conditions and transport pathways during the Transport and Chemical Evolution over the Pacific (TRACE-P) experiment, *J. Geophys. Res.*, **108**(D20), 8782, doi:10.1029/2002JD003092, in press, 2003.
- Jacob, D. J., M. J. Prather, and P. J. Rasch, Evaluation and intercomparison of global atmospheric transport models using ^{222}Rn and other short-lived tracers, *J. Geophys. Res.*, **102**, 5953–5970, 1997.
- Jacob, D. J., J. Crawford, M. M. Kleb, V. S. Connors, R. J. Bendura, J. L. Raper, G. W. Sachse, J. Gille, L. Emmons, and J. C. Heald, Transport and Chemical Evolution over the Pacific (TRACE-P) mission: Design, execution, and first results, *J. Geophys. Res.*, **108**(D20), 8781, doi:10.1029/2002JD003276, in press, 2003.
- Kanakidou, M., F. J. Dentener, and G. P. Brasseur, 3-D global simulations of tropospheric CO distributions—Results of the GIM/IGAC intercomparison 1997 exercise, *Chemosphere*, **1**, 263–282, 1999.
- Lafore, J. P., et al., The Meso-NH atmospheric simulation system. Part I: Adiabatic formulation and control simulations, *Ann. Geophys.*, **16**, 10–90, 1998.
- Lin, S.-J., and R. B. Rood, Multidimensional flux form semi-Lagrangian transport schemes, *Mon. Weather Rev.*, **124**, 2046–2070, 1996.
- Mari, C., et al., One-dimensional modeling of sulfur species during the First Aerosol Characterization Experiment (ACE 1) Lagrangian B, *J. Geophys. Res.*, **104**, 21,733–21,749, 1999.
- Marland, G., T. A. Boden, R. J. Andres, A. L. Brenkert, and C. A. Johnston, Global, regional and national fossil fuel CO_2 emissions, *Tech. Rep.*, U.S. Dept. of Energy, Washington, D. C., 1999.
- Martin, R. V., D. J. Jacob, R. M. Yantosca, M. Chin, and P. Ginoux, Global and regional decreases in tropospheric oxidants from photochemical effect of aerosols, *J. Geophys. Res.*, **108**(D3), 4097, doi:10.1029/2002JD002622, 2003.
- Mauzerall, D. L., J. A. Logan, D. J. Jacob, B. E. Anderson, D. R. Blake, J. D. Bradshaw, B. Heikes, G. W. Sachse, H. Singh, and B. Talbot, Photochemistry in biomass burning plumes and implications for tropospheric ozone over the tropical South Atlantic, *J. Geophys. Res.*, **103**, 8401–8423, 1998.
- McLinden, C. A., S. Olsen, B. Hannegan, O. Wild, M. J. Prather, and J. Sundet, Stratospheric ozone in 3-D models: A simple chemistry and the cross-tropopause flux, *J. Geophys. Res.*, **105**, 14,653–14,665, 2000.
- McRae, G. J., W. R. Goodin, and J. H. Seinfeld, Numerical solution of the atmospheric diffusion equation for chemical reacting flows, *J. Comput. Phys.*, **45**, 1–42, 1982.
- Norwegian Meteorological Institute (EMEP), Transboundary air pollution in Europe part 1: Emissions, dispersion and trends of acidifying and eutrophying agents, *Tech. Rep.*, Oslo, Norway, 1998.
- Organization for Economic Cooperation and Development (OECD), Environmental data compendium, *Tech. Rep.*, location?, 1997.
- Pierce, R. B., D. R. Johnson, F. R. Reames, T. H. Zapolocny, and B. J. Wolf, Numerical investigations with a hybrid isentropic-sigma model, Part I: Normal mode characteristics, *J. Atmos. Sci.*, **48**, 2005–2024, 1991.
- Pierce, R. B., J. A. Al-Saadi, R. S. Eckman, T. D. Fairlie, W. L. Grose, M. M. Kleb, M. Natarajan, and J. R. Olson, Dynamical climatology of the NASA Langley Research Center Interactive Modeling Project for Atmospheric Chemistry and Transport (IMPACT) Model, *J. Geophys. Res.*, **105**, 29,109–29,134, 2000.
- Pochanart, P., H. Akimoto, Y. Kajii, V. M. Potemkin, and T. V. Khodzher, Regional background ozone and carbon monoxide variations in remote Siberia/East Asia, *J. Geophys. Res.*, **108**(D1), 4028, doi:10.1029/2001JD001412, 2003.
- Prather, M. J., Numerical advection by conservation of second-order moments, *J. Geophys. Res.*, **91**, 6671–6681, 1986.
- Rasch, P. J., et al., A comparison of scavenging and deposition processes in global models: Results from the WCRP Cambridge Workshop of 1995, *Tellus*, **52B**, 1025–1056, 2000.
- Sachse, G. W., G. F. Hill, L. O. Wade, and M. G. Perry, Fast-response, high-precision carbon monoxide sensor using a tunable diode laser absorption technique, *J. Geophys. Res.*, **92**, 2071–2081, 1987.
- Spivakovsky, C. M., et al., Climatological distribution of tropospheric OH, *J. Geophys. Res.*, **105**, 8931–8980, 2000.
- Streets, D. G., T. C. Bond, G. R. Carmichael, S. Fernandes, Q. Fu, D. He, Z. Klimont, S. M. Nelson, N. Y. Tsai, M. Q. Wang, J.-H. Woo, and K. F. Yarber, A year-2000 inventory of gaseous and primary aerosol emissions in Asia to support TRACE-P modeling and analysis, *J. Geophys. Res.*, **108**(D21), 8809, doi:10.1029/2002JD003093, in press, 2003.
- Suhre, K., et al., Chemistry and aerosols in the marine boundary layer: 1-D modeling of the three ACE-2 Lagrangian experiments, *Atmos. Environ.*, **34**, 5079–5094, 2000.
- Talbot, R. W., et al., Chemical characterizations of continental outflow over the tropical South Atlantic Ocean from Brazil and Africa, *J. Geophys. Res.*, **101**, 24,187–24,202, 1996.

- Tang, Y., et al., Impacts of aerosols and clouds on photolysis frequencies and photochemistry during TRACE-P: Three-dimensional study using a regional transport model, *J. Geophys. Res.*, 108(D21), 8822, doi:10.1029/2002JD003100, in press, 2003.
- Tripoli, G. J., A nonhydrostatic numerical model designed to simulate scale interaction, *Mon. Weather Rev.*, 125, 120–142, 1997.
- Tulet, P., V. Crassier, F. Solmon, D. Guedalia, and R. Rosset, Description of the mesoscale non hydrostatic chemistry model and application to a transboundary pollution episode between northern France and southern England, *J. Geophys. Res.*, 108(D1), 4021, doi:10.1029/2000JD000301, 2003.
- Verwer, J. G., E. J. Spee, J. G. Blom, and W. H. Hundsdorfer, A second order Rosenbrock method applied to photochemical dispersion problems, *SIAM J. Sci. Comput.*, 20, 1456–1480, 1999.
- Wild, O., and M. J. Prather, Excitation of the primary tropospheric chemical mode in a global 3-D model, *J. Geophys. Res.*, 105, 24,647–24,660, 2000.
- Wild, O., J. Sundet, M. J. Prather, I. Isaksen, H. Akimoto, E. V. Browell, and S. J. Oltmans, CTM ozone simulations for spring 2001 over the western Pacific: Comparisons with TRACE-P lidar, ozonesondes and TOMS columns, *J. Geophys. Res.*, 108(D21), 8826, doi:10.1029/2002JD003283, in press, 2003.
- Woo, J.-H., et al., Contribution of biomass and biofuel emissions to trace gas distributions in Asia during the TRACE-P experiment, *J. Geophys. Res.*, 108(D21), 8812, doi:10.1029/2002JD003200, in press, 2003.
- Yevich, R., and J. A. Logan, An assessment of biofuel use and burning in agricultural waste in the developing world, *Global Biogeochem. Cycles*, 17, doi:10.1029/2002GB001952, in press, 2003.
- Zapotocny, T. H., D. R. Johnson, and F. M. Reames, Development and initial test of the Univ. of Wisconsin global isentropic-sigma model, *Mon. Weather Rev.*, 122, 2160–2178, 1994.
- Zhang, G. J., and N. A. McFarlane, Sensitivity of climate simulations to the parameterization of cumulus convection in the Canadian Climate Centre general circulation model, *Atmos. Ocean*, 33, 407–446, 1995.
- D. J. Allen and K. E. Pickering, Department of Meteorology, University of Maryland, College Park, MD 20742, USA. (allen@atmos.umd.edu; pickerin@atmos.umd.edu)
- G. R. Carmichael and Y. Tang, Center for Global and Regional Environmental Research and Department of Chemical and Biochemical Engineering, University of Iowa, Iowa City, IA 52242, USA. (gcarmich@icaen.uiowa.edu; ytang@cgrer.uiowa.edu)
- T. D. Fairlie, D. J. Jacob, J. A. Logan, and P. I. Palmer, Harvard University, Pierce Hall, 29 Oxford Street, Cambridge, MA 02318, USA. (tdf@io.harvard.edu; djacob@fas.harvard.edu; jal@io.harvard.edu; pip@io.harvard.edu)
- H. E. Fuelberg and C. M. Kiley, Department of Meteorology, Florida State University, 404 Love Building, Tallahassee, FL 32306-4520, USA. (fuelberg@huey.met.fsu.edu; ckiley@huey.met.fsu.edu)
- C. Mari, Laboratoire d'Aerologie, UMR CNRS/Universite Paul Sabatier, 14 avenue Edouard Belin, 31400 Toulouse, France. (marc@aero.obs-mip.fr)
- R. B. Pierce and G. W. Sachse, NASA Langley Research Center, Hampton, VA 23681, USA. (r.b.pierce@larc.nasa.gov; g.w.sachse@larc.nasa.gov)
- T. K. Shaack, Space Science and Engineering Center, University of Wisconsin, Madison, WI, USA.
- D. G. Streets, Argonne National Laboratory, 9700 S. Cass Ave., Argonne, IL 60439, USA. (dstreets@anl.gov)
- O. Wild, Frontier Research System for Global Change, 3173-25 Showa-machi, Kanazawa-ku, Yokohama, Kanagawa 236-0001, Japan. (oliver@jamstec.go.jp)

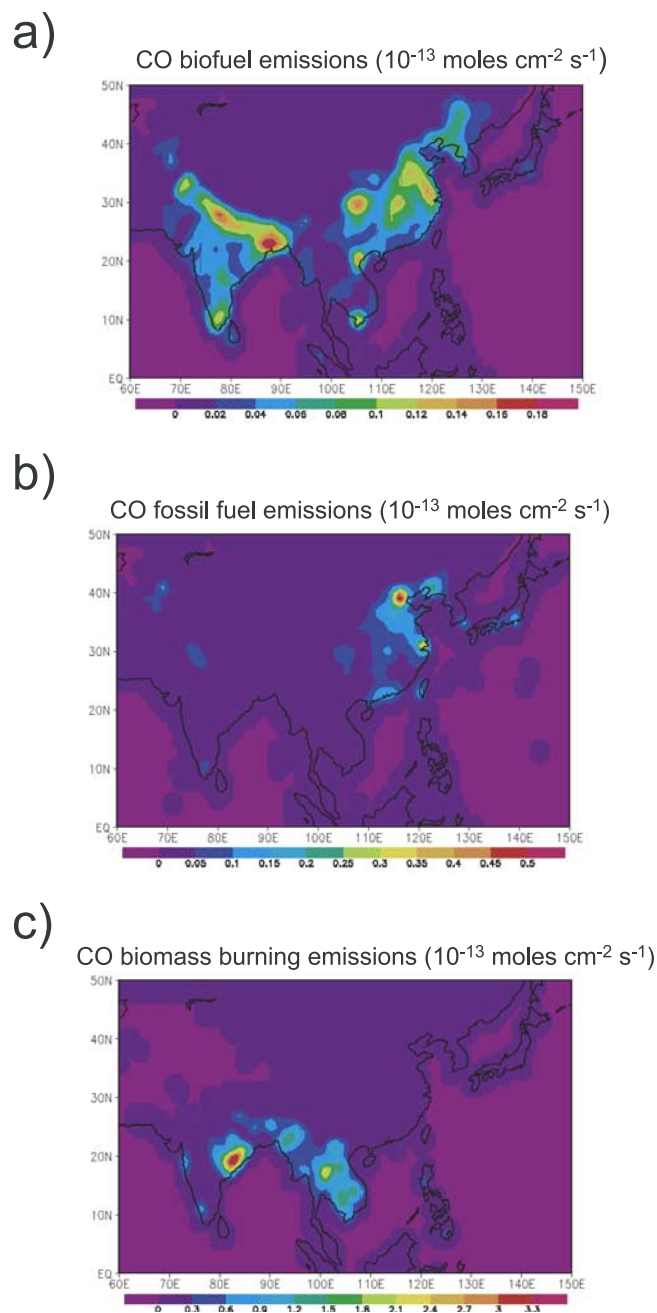


Figure 1. CO emissions used by all CTMs in this study from (a) biofuels, (b) fossil fuels, and (c) biomass burning.

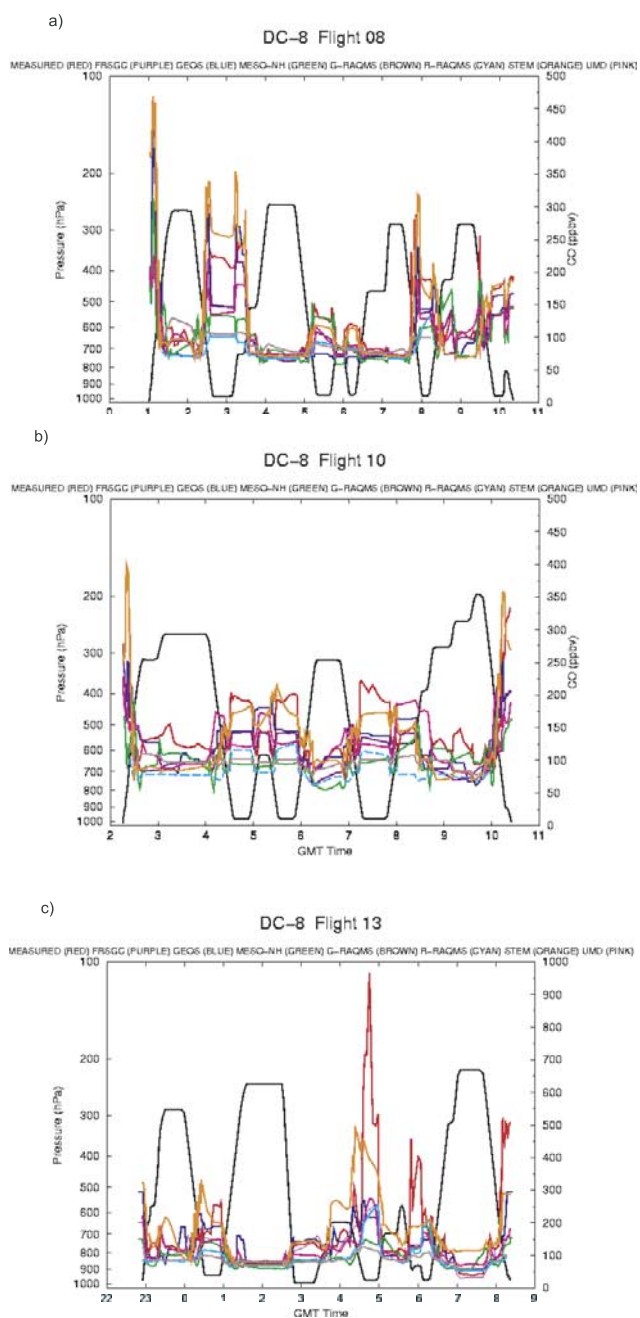
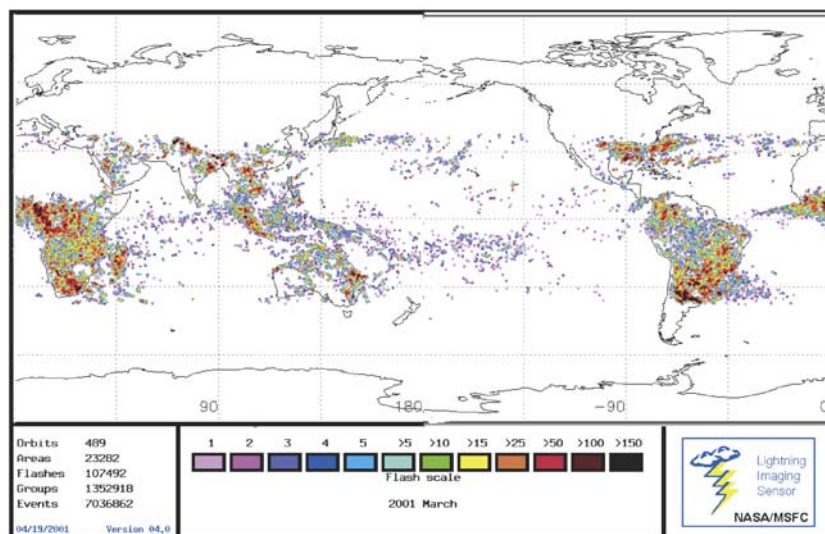


Figure 3. Time series of aircraft altitude (black), aircraft-derived CO (red), and the seven model-derived simulations for (a) DC-8 flight 8, (b) DC-8 flight 10, and (c) DC-8 flight 13. FRSGC/UCI (violet), GEOS-CHEM (blue), Meso-NH (green), RAQMS Global (brown), RAQMS Regional (cyan), STEM (orange), UMD CTM (pink).

a)



b)

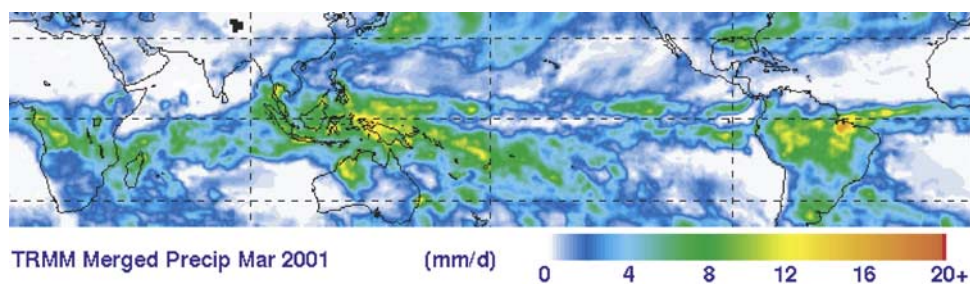
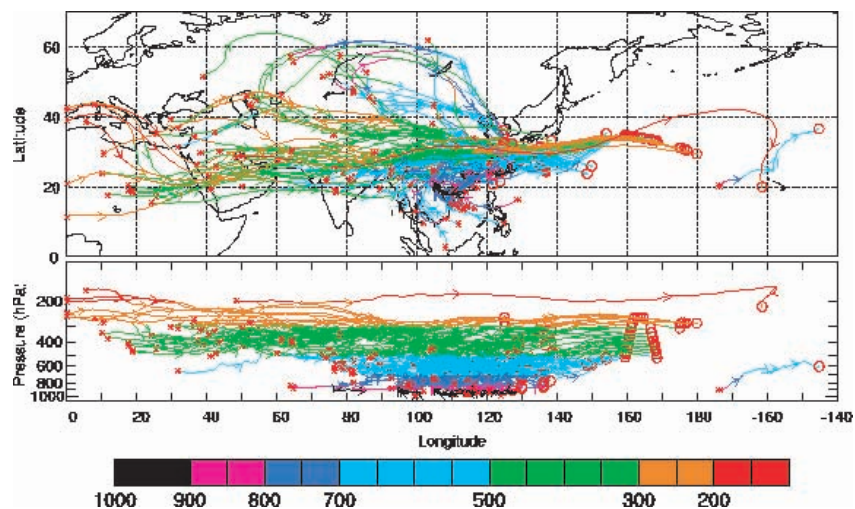


Figure 7. (a) Lightning data for March 2001 from the Lightning Imaging Sensor (LIS) (b) Precipitation data for March 2001 from the Tropical Rainfall Measuring Mission (TRMM).

a)

TRACE-P 5 Day Backward Trajectories
FRSGC/UCI CO Error > 50 ppbv



b)

TRACE-P 5 Day Backward Trajectories
FRSGC/UCI CO Error < - 100 ppbv

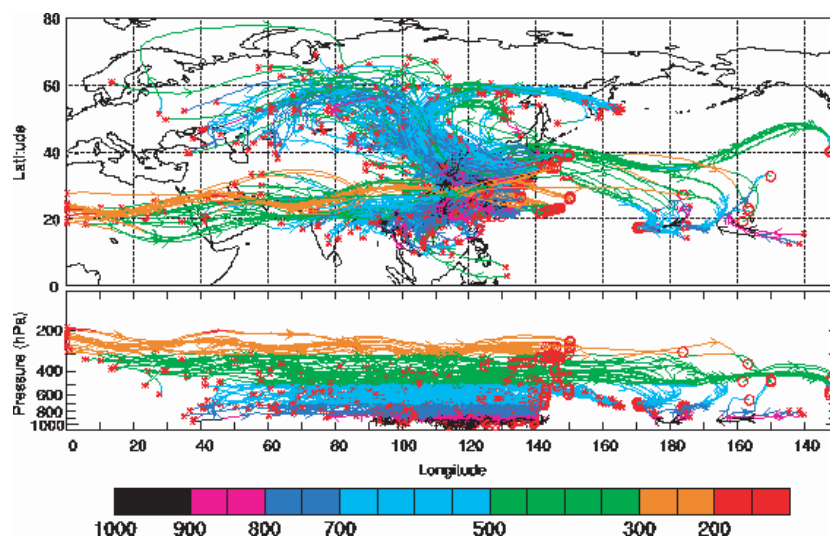


Figure 9. Five-day backward trajectories for the combination of DC-8 flights 7–17 based on FRSGC/UCI model CO error. (a) FRSGC/UCI model CO is greater than aircraft-derived CO by 50 ppbv or more, (b) FRSGC/UCI model CO is less than aircraft-derived CO by 100 ppbv or more.

TRACE-P 5 Day Backward Trajectories
DC-8 Flight 15

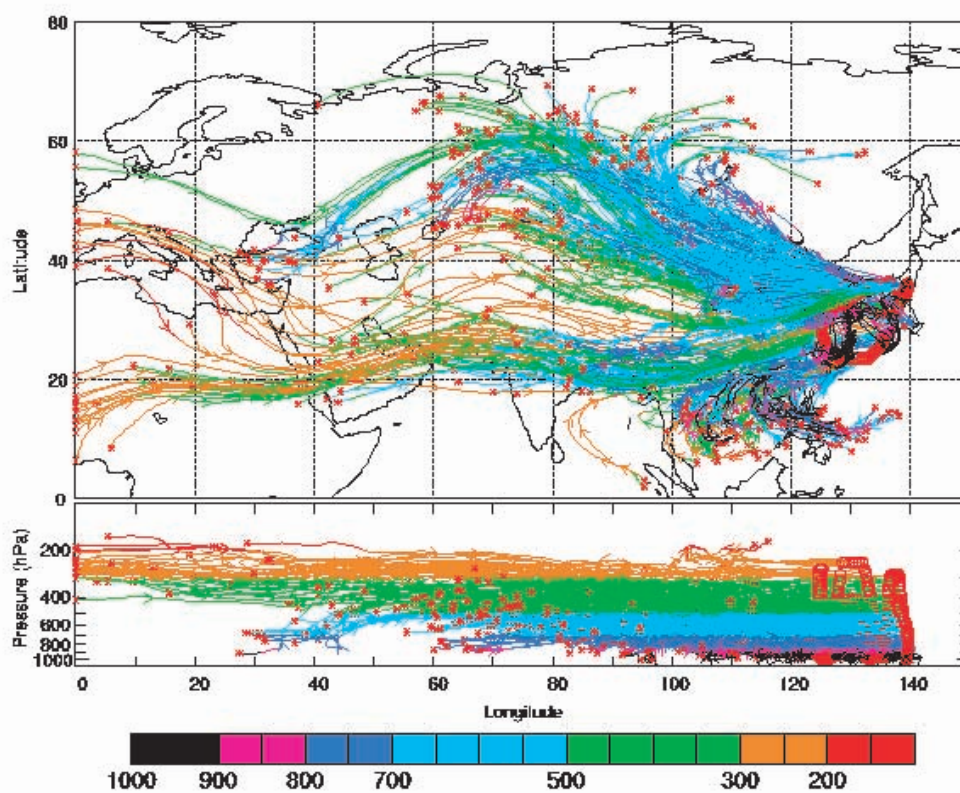
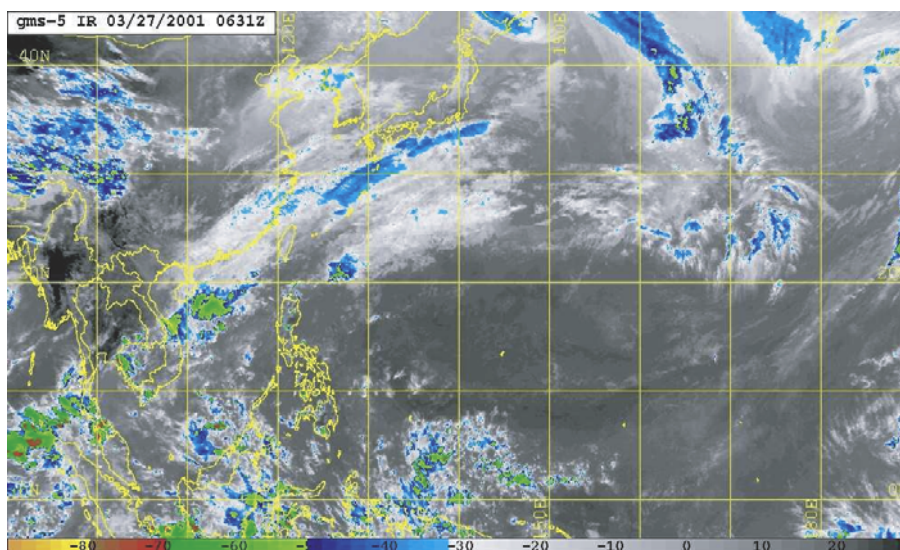


Figure 11. Five-day backward trajectories for DC-8 flight 15.

a)



b)

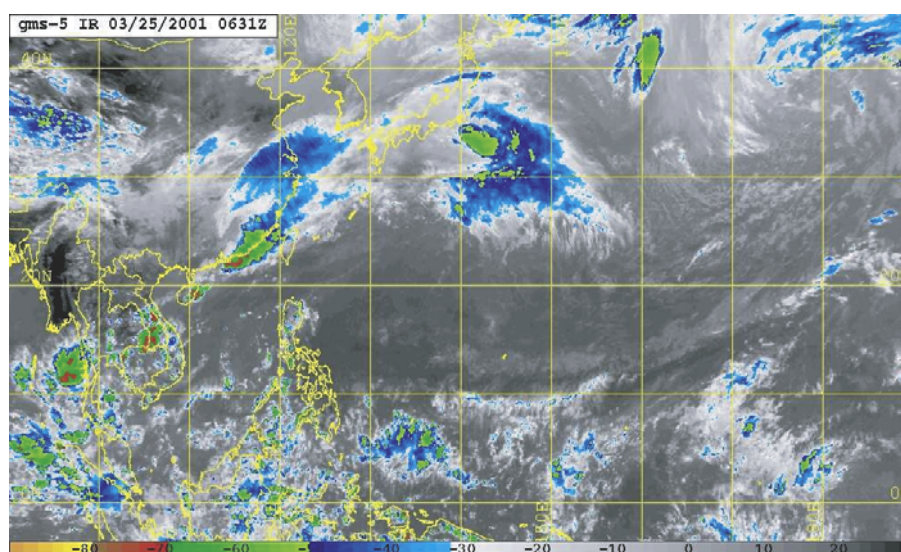
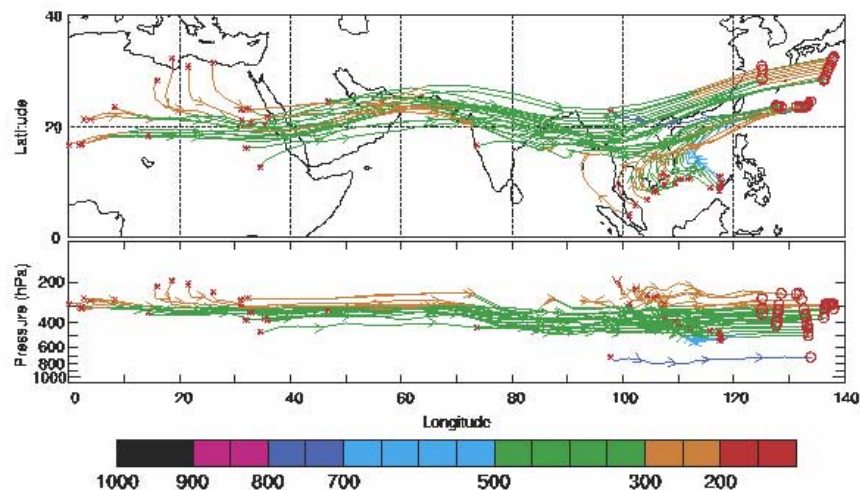


Figure 12. Infrared imagery from Geostationary Meteorological Satellite (GMS) 5 (a) at the time of flight 15 (0631 UTC 27 March) and (b) two days prior to flight 15 (0631 UTC 25 March).

a)

TRACE-P 5 Day Backward Trajectories
 GEOS-CHEM CO Error > 50 ppbv



b)

TRACE-P 5 Day Backward Trajectories
 GEOS-CHEM CO Error < - 100 ppbv

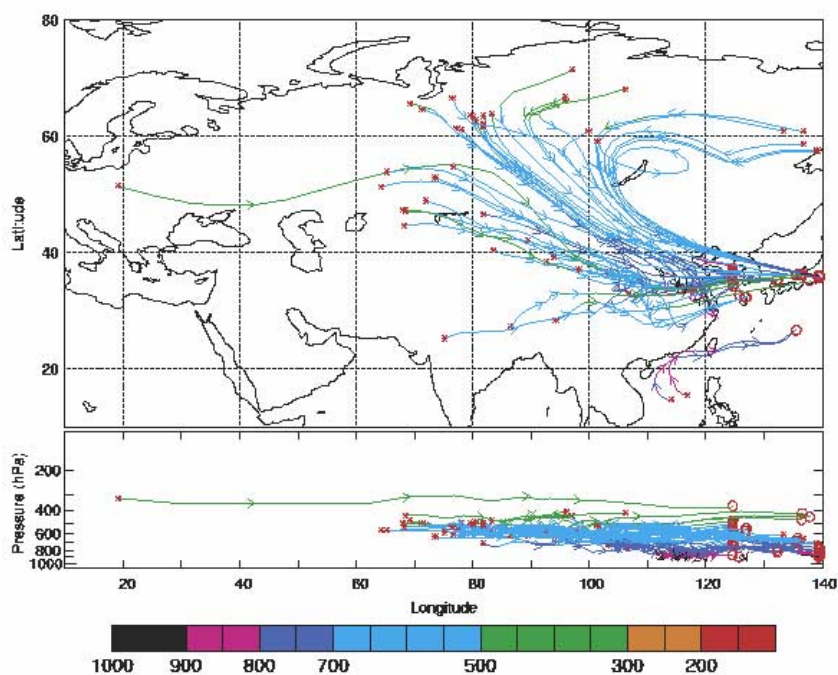


Figure 13. Five-day backward trajectories for DC-8 flight 15 based on GEOS-CHEM model CO error. (a) GEOS-CHEM model CO is greater than aircraft-derived CO by 50 ppbv or more, (b) GEOS-CHEM model CO is less than aircraft-derived CO by 100 ppbv or more.

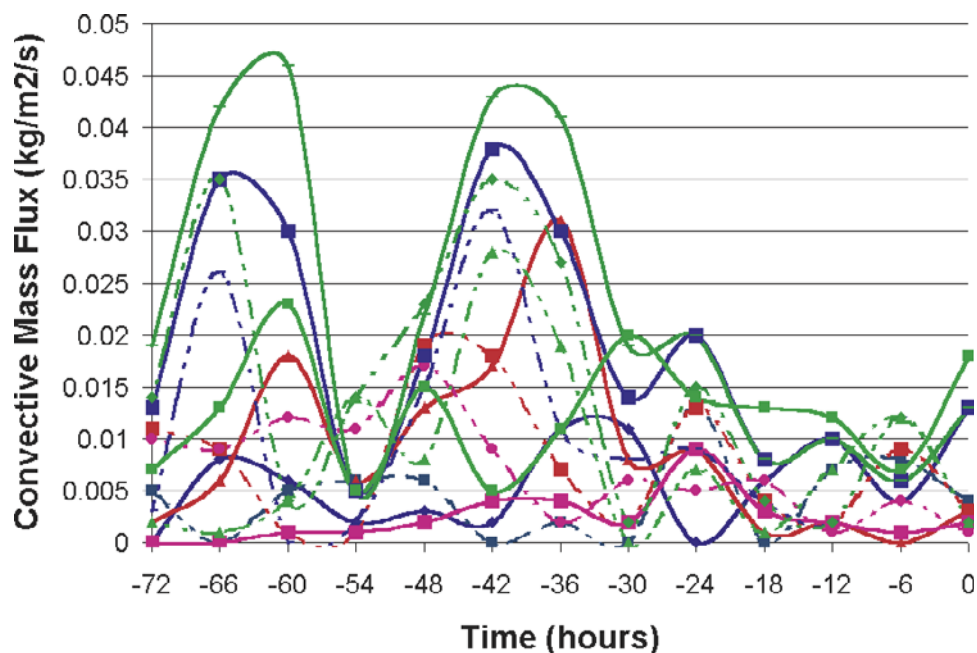


Figure 14. Convective mass flux at 6 hourly intervals for six representative trajectories based on GEOS-CHEM CO exceeding the measured value by 50 ppbv or more during DC-8 flight 15. Results are shown for GEOS-CHEM (solid line) and FRSGC/UCI (dashed line). The color of each line indicates the specific trajectory. Thus each color is used in two lines indicating the same starting point along the flight track (one for GEOS-CHEM and one for FRSGC/UCI).

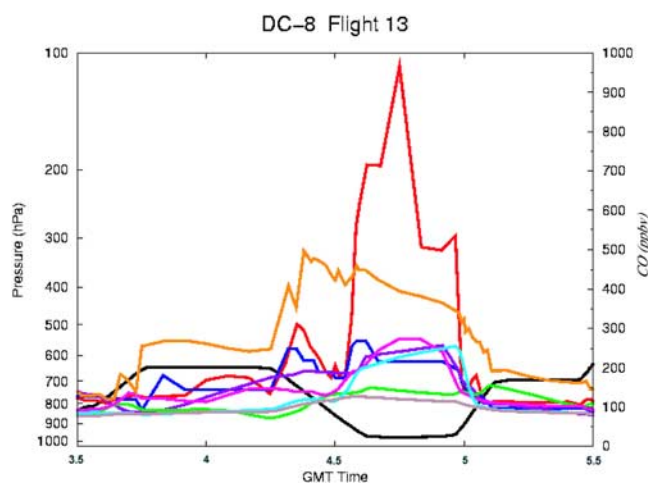


Figure 17. Time series of aircraft altitude (black), aircraft-derived CO (red), and the seven model-derived simulations during the sampling of the Shanghai plume by DC-8 flight 13. FRSGC/UCI (violet), GEOS-CHEM (blue), Meso-NH (green), RAQMS-Global (brown), RAQMS-Regional (cyan), STEM (orange), and UMD CTM (pink).